

Aethalometer multiple scattering correction C_{ref} for mineral dust aerosols

Claudia Di Biagio¹, Paola Formenti¹, Mathieu Cazaunau¹, Edouard Pangui¹, Nicolas Marchand², and Jean-François Doussin¹

¹ Laboratoire Interuniversitaire des Systèmes Atmosphériques (LISA), UMR 7583, CNRS, Université Paris Est Créteil et Université Paris Diderot, Institut Pierre et Simon Laplace, Créteil, France

² Aix Marseille Univ., CNRS, LCE, Marseille, France

Correspondence to: C. Di Biagio (cldibiagio@gmail.com) and P. Formenti (paola.formenti@lisa.u-pec.fr)

Abstract

In this study we provide a first estimate of the aethalometer multiple scattering correction C_{ref} for mineral dust aerosols. C_{ref} is an empirical constant used to correct the aerosol absorption coefficient measurements for the multiple scattering artefact of the aethalometer, i.e. the filter fibres on which aerosols are deposited scatter light and this is miscounted as absorption. The C_{ref} at 450 and 660 nm was obtained from the direct comparison of aethalometer data (Magee Sci. AE31) with the absorption coefficient calculated as the difference between the extinction and scattering coefficients measured by a Cavity Attenuated Phase Shift Extinction analyzers (CAPS PMex) and a nephelometer respectively at 450 nm and the absorption coefficient from a MAAP (Multi-Angle Absorption Photometer) at 660 nm. Measurements were performed on seven dust aerosol samples generated in the laboratory by the mechanical shaking of natural parent soils issued from different source regions worldwide. The single scattering albedo (SSA) at 450 and 660 nm and the size distribution of the aerosols were also measured.

C_{ref} for mineral dust varies between 1.81 and 2.56 for a SSA of 0.85–0.96 at 450 nm and between 1.75 and 2.28 for a SSA of 0.98–0.99 at 660 nm. The calculated mean and one standard deviation C_{ref} for dust is 2.09 (\pm 0.22) at 450 nm and 1.92 (\pm 0.17) at 660 nm. With this new C_{ref} the dust absorption coefficient by aethalometer is about 2% (450 nm) and 11% (660 nm) higher than that obtained by using $C_{ref}=2.14$ at both 450 and 660 nm, as usually assumed in the literature. This difference induces up to 3% change in the dust SSA at 660 nm. The C_{ref} seems independent of the particle fine and coarse size fractions, and so the obtained C_{ref} can be applied to dust both close to sources and following transport. Additional experiments performed with pure kaolinite mineral and polluted ambient aerosols indicate a C_{ref} of 2.49 (\pm 0.02) and 2.32 (\pm 0.01) at 450 and 660 nm respectively (SSA=0.96–0.97) for kaolinite, and a C_{ref} of 2.32 (\pm 0.36) at 450 nm and 2.32 (\pm 0.35) at 660 nm for pollution aerosols (SSA=0.62–0.87 at 450 nm and 0.42–0.76 at 660 nm).

37 1. Introduction

38 Abundant and widespread in the atmosphere, mineral dust strongly contributes to the global and
39 regional direct radiative effect and climate forcing (Highwood and Ryder, 2014; Miller et al., 2014).
40 Mineral dust interacts through processes of scattering and absorption with both incoming shortwave
41 radiation and outgoing terrestrial longwave radiation (Sokolik and Toon, 1999). Currently, the
42 evaluation of the direct effect of mineral dust and its climate implications is still limited by the
43 knowledge of the intensity of the dust absorption in the shortwave spectral range (Miller et al., 2004;
44 Balkanski et al., 2007; Solmon et al., 2008; Jin et al., 2016), represented by the light absorption
45 coefficient (β_{abs} , units of Mm^{-1}). The absorption coefficient of mineral dust accounts for less than ~10-
46 20% of its total shortwave extinction, where it shows a pronounced spectral variation (Cattrall et al.,
47 2003; Redmond et al., 2010). The highest dust absorption occurs in the UV-VIS region of the
48 spectrum, while it levels off to null values towards the near IR (Caponi et al., 2017). As a result, its
49 single scattering albedo (SSA), i.e. the ratio of the aerosol scattering (β_{sca}) to extinction ($\beta_{\text{ext}}=\beta_{\text{sca}}+\beta_{\text{abs}}$)
50 coefficient, increases from values of ~0.80-0.90 at 370 nm to values of ~0.95-0.99 at 950 nm (e.g.,
51 Schladitz et al., 2009; Redmond et al., 2010; Formenti et al., 2011; Ryder et al., 2013).

52 Given its relatively high SSA, mineral dust can be considered as weakly absorbing in the shortwave.
53 This is particularly true when compared to other aerosol species, such as soot, for which the SSA in
54 the visible may be as low as 0.2 (Bergstrom et al., 2007). Nonetheless, because of its elevated
55 atmospheric concentration (~100-100000 $\mu\text{g m}^{-3}$ close to sources and ~0.1-100 $\mu\text{g m}^{-3}$ after mid- to
56 intercontinental transport; e.g., Goudie and Middleton, 2006; Kandler et al., 2009; Querol et al., 2009;
57 Denjean et al., 2016a), light absorption by mineral dust can be comparable to that of soot both at
58 regional and global scales (Reddy et al., 2005; Caponi et al., 2017). Under very intense dust
59 episodes, dust may absorb up to ~150 Wm^{-2} of incoming solar radiation (Slingo et al., 2006; di Sarra
60 et al., 2011), inducing a remarkable warming of the atmospheric layer. This strong warming can alter
61 the atmospheric structure and stability (Heinold et al., 2008), with a possible influence on the
62 atmospheric dynamics and meteorological fields (Pérez et al., 2006). By its direct shortwave effect
63 dust also affects the position of the Inter Tropical Convergence Zone, which in turn influences the
64 Western African Monsoon and modifies the pattern and intensity of rainfall over Northern Africa and
65 the Sahel (Yoshioka et al., 2007). Nonetheless, the extent of the dust effect and its implications
66 critically depend on the exact amount of absorbed shortwave radiation. Solmon et al. (2008), for
67 example, showed that a small change (5%) in the shortwave SSA of dust may modify the effect of
68 dust on the Western African Monsoon, moving from a reduction to an increase of precipitation over
69 the Sahel.

70 The accurate estimation of the dust absorption over the whole shortwave range is therefore
71 necessary to properly assess its direct radiative effect and climate implications. One instrument used
72 to obtain aerosol-light absorption from the UV to near IR range is the aethalometer (Magee Sci. AE31
73 model, Hansen et al., 1984; Arnott et al., 2005), operating at seven wavelengths in the 370–950 nm
74 range. The aethalometer reports equivalent black carbon mass concentration but the spectral
75 absorption by aerosols can be also calculated. Given its large spectral interval, the aethalometer has

76 been used in the past to investigate the spectral dependence of dust absorption (Fialho et al., 2005;
77 Formenti et al., 2011), as well as the absorption by many aerosol types in different environments
78 (Sandradewi et al., 2008; Segura et al., 2014; Di Biagio et al., 2016; Backman et al., 2016). General
79 reviews on aerosol absorption measurements and their applications are provided by Horvath (1993)
80 and Moosmüller et al. (2009).

81 The working principle of the aethalometer, a filter-based instrument, consists in measuring the
82 attenuation through an aerosol-laden quartz filter according to the Beer-Lambert law, used then to
83 derive the spectral attenuation coefficient (β_{ATT}) of the deposited particles (Hansen et al., 1984). The
84 “true” spectral aerosol absorption coefficient (β_{abs}) is proportional but lower than β_{ATT} (Weingartner et
85 al., 2003; Collaud Coen et al., 2010; hereinafter referred as W2003 and C2010), because β_{ATT} is
86 enhanced by (i) aerosol scattering towards directions different from that of the detector (scattering
87 effect); (ii) gradual accumulation of absorbing particles on the loaded filter, thus reducing the optical
88 path (loading effect); (iii) multiple scattering of the light beam by the filter fibres, increasing the optical
89 path (multiple scattering effect).

90 Empirical formulations of the scattering and loading effects are available in the literature and permit
91 the correction of aethalometer data for these artefacts (W2003; Arnott et al., 2005; Schmid et al.,
92 2006; Virkkula et al., 2007; C2010). The correction of the multiple scattering effect instead requires
93 the knowledge of a correction factor C_{ref} , which needs to be directly estimated by comparison of
94 aethalometer data against reference absorption measurements (W2003; C2010).

95 Currently data for C_{ref} are available for soot particles ($C_{\text{ref}}=2.1-2.2$ at 660 nm, W2003), internally and
96 externally mixed soot particles and organic material ($C_{\text{ref}}=2.3-3.9$, W2003), and ambient aerosols
97 collected in Europe and Amazonia ($C_{\text{ref}}=2.6-4.8$, C2010; $C_{\text{ref}}=4.9-6.3$, Saturno et al., 2016) and in the
98 Arctic ($C_{\text{ref}}=3.1$, Backman et al., 2016). The value most often used in the literature is 2.14 (± 0.21),
99 assumed as wavelength-independent (e.g., Sandradewi et al., 2008; Formenti et al., 2011; Di Biagio
100 2016), which corresponds to the mean of observations at 660 nm for soot aerosols (W2003). Both
101 W2003 and C2010, however, found a dependence of C_{ref} on the aerosol single scattering albedo, with
102 C_{ref} decreasing for increasing SSA. Thus, the value of 2.14 obtained for highly absorbing soot
103 (SSA ~ 0.2 in the visible) may not be appropriate for weakly absorbing mineral dust.

104 Henceforth, in this work we present the experimental estimate of C_{ref} for mineral dust aerosols at 450
105 and 660 nm obtained from a laboratory-based intercomparison study. Experiments were conducted
106 on seven dust aerosol samples generated by the mechanical shaking of natural parent soils. Control
107 experiments on pure kaolinite mineral, ambient aerosols sampled in the polluted environment of the
108 suburbs of Paris, and purely scattering ammonium sulfate, were also performed to investigate the
109 dependence of C_{ref} on the aerosol single scattering albedo.

110 **2. Experimental set-up**

111 The experimental set-up used for the intercomparison study is shown in **Fig. 1**. Instrumental details
112 and uncertainties are summarized in **Table 1**. The following measurements were performed from a 8-
113 port glass manifold (~ 1 L volume):

114 - the absorption coefficient (β_{abs}) by a 7-wavelength aethalometer (Magee Sci., model AE31 working
115 at 370, 470, 520, 590, 660, 880, 950 nm; flowrate 8 L min⁻¹, 2-min resolution) and a MAAP (Multi-
116 Angle Absorption Photometer, Thermo Sci., model 5012 working at 670 nm; flowrate 8 L min⁻¹, 1-
117 min resolution). Unlike the aethalometer, the MAAP measures the transmitted light from the
118 aerosol-laden filter and also the backscattered light at two angles (135° and 165°) (Petzold et al.,
119 2005). Backscattering measurements are used to constrain the scattering fraction of the measured
120 attenuation that would erroneously be interpreted as absorption. The aerosol absorption coefficient
121 for the MAAP is obtained from a radiative transfer scheme taking into account the multiple
122 scattering in the filter and the scattering effect, without requiring any further adjustment (Petzold
123 and Schönlinner, 2004). The MAAP is commonly assumed to provide the most reliable filter-based
124 direct estimate of the aerosol absorption coefficient at a single wavelength (Andreae and Gelècser
125 2006). In this study we assume for the MAAP the manufacturer's reported wavelength of 670 nm,
126 although Müller et al. (2011) measured for this instrument a wavelength of 637 nm. An estimate of
127 the change in the obtained C_{ref} due to the change in MAAP nominal wavelength from 670 to 637
128 nm is reported in Sect. 4.2;

129 - the scattering coefficient (β_{sca}) in the 7-170° angular range by a 3-wavelength nephelometer (TSI
130 Inc., model 3563 working at 450, 550 and 700 nm; flowrate 18 L min⁻¹, 1-s resolution);

131 - the extinction coefficient (β_{ext}) by two Cavity Attenuated Phase Shift Extinction analyzers (CAPS
132 PMex by Aerodyne, one working at 450 nm and the other at 630 nm; flowrate 0.85 L min⁻¹, 1-s
133 resolution);

134 - the particle number size distribution (dN/dlogD) by a scanning mobility particle sizer, SMPS, (TSI
135 Inc., DMA Model 3080, CPC Model 3772; operated at 2.0/0.2 L min⁻¹ sheath/aerosol flow rates; 3-
136 min resolution) and an optical particle counter, OPC, (Grimm Inc., model 1.109, 655 nm operating
137 wavelength; flowrate 1.2 L min⁻¹, 6-s resolution). The SMPS measures the aerosol number
138 concentration in the electrical mobility diameter (D_m) range 0.019–0.882 μm , and the OPC
139 measures in the optical equivalent diameter (D_{opt}) range 0.25–32 μm .

140 Sampling lines from the manifold to the instruments were made of conductive silicone tubing (TSI Inc.,
141 $6.4 \cdot 10^{-3}$ m diameter) to minimize particle loss by electrostatic deposition. They were designed to be as
142 straight and as short as possible. Their length, varying between 0.3 and 0.7 m, was adjusted based
143 on the flowrate of each instrument to ensure an equivalent particle loss, so that the same aerosol size
144 distribution was in input to the different instruments. Particular care was given to ensure the same
145 aerosol size at the input of the aethalometer and the MAAP. To this end, as illustrated in Fig. 1, the
146 two instruments sampled air from the same manifold exit line, and also the same sampling flow rate
147 was set for the two instruments (8 L min⁻¹). Particle loss calculations were performed with the Particle
148 Loss Calculator (PLC) software (von der Weiden et al., 2009).

149 Aerosols were generated in three ways:

150 - mineral dust was generated by mechanical shaking as described and validated in Di Biagio et al.
151 (2014, 2017). About 3 gr of soil sample (sieved at 1000 μm and dried at 100°C) was placed in a

152 Büchner flask and shaken at 100 Hz by a sieve shaker (Retsch AS200). The dust was injected in the
153 manifold by a flow of N₂ at 3.5 L min⁻¹ through a single-stage impactor used to eliminate particles
154 larger than about 20 µm, which could be preferentially sampled by the instruments with the highest
155 flow rate. Pure N₂ was added to the aerosol flow to make the injection flow equal to the total sampling
156 flow by instruments connected to the manifold (about 38 L min⁻¹);

157 - ammonium sulfate (Sigma-Aldrich 99.999% purity, 0.03 M solution in ultrapure water) and kaolinite
158 particles (Source Clay Repository KGa-2, 0.05 M solution in ultrapure water) were generated by a
159 constant flow atomizer (TSI, model 3075) operated at 3 L min⁻¹ and coupled with a diffusion drier (TSI,
160 model 3062). As for dust, pure N₂ was added to the aerosol flow to equalize the total sampling flow;

161 - ambient pollution aerosols were sampled by opening the manifold to the exterior ambient air.
162 Ambient aerosols were not dried before entering the manifold. Sampling was performed at the
163 University Paris-Est Creteil, in the suburbs of Paris, at the ground floor of the University building,
164 which is close to a main local road (~20 m) and to the A86 highway (~200 m).

165 **3. Strategy for data analysis**

166 The aethalometer spectral attenuation coefficient $\beta_{ATT}(\lambda)$ is related to the measured attenuation
167 $ATT(\lambda)$ through the following formula:

$$168 \quad \beta_{ATT}(\lambda) = \frac{\Delta ATT(\lambda) A}{\Delta t V} \quad (1)$$

169 where A is the area of the aerosol collection spot (0.5 ± 0.1) cm² and V the air sampled volume (0.016
170 m³ over 2-min integration time). $\Delta ATT(\lambda)/\Delta t$ in Eq. (1) can be calculated as the linear fit of the
171 measured attenuation as a function of time.

172 The spectral attenuation coefficient $\beta_{ATT}(\lambda)$ measured by the aethalometer is related to the targeted
173 absorption coefficient $\beta_{abs}(\lambda)$ by the following formula (C2010):

$$174 \quad \beta_{abs}(\lambda) = \frac{\beta_{ATT}(\lambda) - \alpha(\lambda)\beta_{sca}(\lambda)}{R \cdot C_{ref}} \quad (2)$$

175 where the different terms parametrise different instrument artefacts:

176 - the scattering effect $\alpha(\lambda)\beta_{sca}(\lambda)$, that is, the amount of scattered radiation by the aerosols deposited
177 on the filter that is miscounted as absorption, where $\alpha(\lambda)$ is a wavelength-dependent proportionality
178 constant and $\beta_{sca}(\lambda)$ is the aerosol spectral scattering coefficient;

179 - the loading effect R, representing the artificial flattening of measured attenuation with time due to the
180 gradual accumulation of absorbing particles on the loaded filter;

181 - the multiple scattering C_{ref} , representing multiple scattering of the light beam by the filter fibres.

182 The $\alpha(\lambda)$ term and R in Eq. (2) can be calculated through various empirical formulas reported in the
183 literature (W2003, Arnott et al., 2005; Virkkula et al., 2007; Schmid et al., 2006; C2010). The
184 determination of C_{ref} , instead, is the objective of our study.

185 3.1. Scattering effect correction

186 Arnott et al. (2005) provide for $\alpha(\lambda)$ the following formulation:

$$187 \quad \alpha(\lambda) = A^{d-1} \cdot c \cdot \lambda^{-\alpha_s(d-1)} \quad (3)$$

188 where the A and α_s terms are obtained from the power-law fit of $\beta_{\text{sca}}(\lambda)$ versus λ , and the c and d
189 terms can be determined from the power-law fit of the attenuation $\beta_{\text{ATT}}(\lambda)$ versus the scattering $\beta_{\text{sca}}(\lambda)$
190 coefficient as

$$191 \quad \beta_{\text{sca}}(\lambda) = A \lambda^{-\alpha_s} \quad (4)$$

$$192 \quad \beta_{\text{ATT}}(\lambda) = c \beta_{\text{sca}}(\lambda)^d \quad (5)$$

193 3.2. Loading effect correction

194 Two formulations for the loading effect correction R are proposed by W2003 and C2010:

$$195 \quad R(\text{W2003})(\lambda) = \left(\frac{1}{f(\lambda)} - 1 \right) \frac{\ln(\text{ATT}(\lambda)) - \ln(10\%)}{\ln(50\%) - \ln(10\%)} + 1 \quad (6a)$$

$$196 \quad R(\text{C2010})(\lambda) = \left(\frac{1}{f(\lambda)} - 1 \right) \frac{\text{ATT}(\lambda)}{50\%} + 1 \quad (6b)$$

197 The factor $f(\lambda)$ represents the dependence of the loading effect on the aerosol absorption. This
198 dependence is parametrized by the aerosol single scattering albedo $\text{SSA}(\lambda)$ in the form of

$$199 \quad f(\lambda) = a(1 - \text{SSA}(\lambda)) + 1 \quad (7)$$

200 where a, equal to 0.85 in W2003 and 0.74 in C2010, is obtained as the slope of the linear fit between
201 the attenuation coefficient β_{ATT} normalized to its value at 10% attenuation ($\beta_{\text{ATT}}/\beta_{10\%}$) and the natural
202 logarithm of the measured attenuation $\ln(\text{ATT}(\lambda))$.

203 3.3. Multiple scattering correction

204 For the determination of C_{ref} only β_{ATT} and R are required. Henceforth in this work, attenuation data
205 from the aethalometer were corrected for the loading effect R but not for the scattering term
206 $\alpha(\lambda)\beta_{\text{sca}}(\lambda)$. Three different formulations of C_{ref} were therefore considered:

$$207 \quad C_{\text{ref}}^*(\lambda) = \frac{\beta_{\text{ATT}}(\lambda)}{\beta_{\text{abs-ref}}(\lambda)} \quad (8a)$$

$$208 \quad C_{\text{ref}}(\text{W2003})(\lambda) = \frac{1}{\beta_{\text{abs-ref}}(\lambda)} \frac{\beta_{\text{ATT}}(\lambda)}{R(\text{W2003})(\lambda)} \quad (8b)$$

$$209 \quad C_{\text{ref}}(\text{C2010})(\lambda) = \frac{1}{\beta_{\text{abs-ref}}(\lambda)} \frac{\beta_{\text{ATT}}(\lambda)}{R(\text{C2010})(\lambda)} \quad (8c)$$

210 The $\beta_{\text{abs-ref}}$ term in Eq. 8a-8c represents the reference absorption coefficient estimated from
 211 independent measurements. C_{ref}^* does not take into account the loading effect correction in
 212 aethalometer data, as done by Schmid et al. (2006). $C_{\text{ref}}(\text{W2003})$ and $C_{\text{ref}}(\text{C2010})$ take this correction
 213 into account, by using the $R(\text{W2003})$ and the $R(\text{C2010})$ parametrisations, respectively. The spectral
 214 $\beta_{\text{ATT}}/R(\text{C2010})$ was used to calculate the absorption Ångström exponent (α_A). Note that in this work
 215 we considered, for each experiment, only data corresponding to $\text{ATT} < 20\%$ to calculate β_{ATT}
 216 ($R^2 > 0.99$ for the $\Delta\text{ATT}/\Delta t$ fits in all cases, see Eq. (1)). This threshold was fixed based on two
 217 requirements: first, we limited our data analysis to points with low attenuation in order to account
 218 almost exclusively for the scattering by the filter fibers in the C_{ref} calculation and not for the scattering
 219 from aerosol particles embedded in the filter. This choice was done also for consistency with the
 220 literature, since both W2003 and C2010 relate C_{ref} to $\text{ATT} \sim 10\%$. Second, this choice ensured that
 221 enough data points were available for analysis regardless of the aerosol type, in particular for ambient
 222 aerosols, for which attenuation rapidly exceeded 10%.

223 3.4. Determination of reference absorption coefficient and single scattering albedo

224 The reference absorption coefficient $\beta_{\text{abs-ref}}$ in Eq. 8a-8c was obtained in different ways depending on
 225 wavelength. At 450 nm, $\beta_{\text{abs-ref}}$ was obtained with the “extinction minus scattering” approach by using
 226 the CAPS measurements for extinction and the nephelometer measurements for scattering. At 660
 227 nm, $\beta_{\text{abs-ref}}$ was extrapolated from MAAP measurements at 670 nm.

228 3.4.1. Direct determination of reference absorption coefficient at 660 nm from the MAAP

229 The reference absorption coefficient $\beta_{\text{abs-ref}}$ at 660 nm was obtained by the MAAP measurement at
 230 670 nm. The MAAP attenuation (ATT) at 670 nm is estimated from the measured transmission (T)
 231 and retrieved single scattering albedo of the aerosol-filter layer (SSA_0 , from the inversion algorithm)
 232 as

$$233 \quad \text{ATT}(670) = (1 - \text{SSA}_0) \cdot \ln T \cdot 100 \quad (9)$$

234 Equation (1) is applied to estimate the absorption coefficient at 670 nm from $\text{ATT}(670)$. The area of
 235 the aerosol collection spot is 2 cm^2 and the sampled volume is 0.008 m^3 over 1-min integration time.
 236 The absorption coefficient of the MAAP was extrapolated to the 660 nm wavelength by using the
 237 absorption Ångström exponent α_A calculated from aethalometer data.

238 3.4.2. Indirect determination of reference absorption coefficient at 450 nm: "extinction minus 239 scattering" approach

240 The reference absorption coefficient $\beta_{\text{abs-ref}}$ at 450 nm was calculated as the difference between the
 241 extinction and scattering coefficient from the CAPS and the nephelometer.

242 The extinction coefficient β_{ext} at 450 and 630 nm was measured directly by the two CAPS analyzers
 243 without additional corrections (Massoli et al., 2010). The spectral β_{ext} was used to calculate the
 244 extinction Ångström exponent (α_E), applied then to extrapolate β_{ext} at 660 nm.

245 The scattering coefficient β_{sca} at 450, 550, and 700 nm measured by the nephelometer between 7 and
 246 170° was corrected for the size-dependent angular truncation of the sensing volume to report it to the
 247 full angular range 0°-180° (Anderson and Ogren, 1998). Two different approaches were used: for sub-
 248 micrometric ammonium sulfate, the correction proposed by Anderson and Ogren (1998) was applied,
 249 while for aerosols with a significant coarse fraction (dust, ambient air and kaolinite), the truncation
 250 correction was estimated by optical calculations according to the Mie theory for homogeneous
 251 spherical particles using as input the measured number size distribution. In the calculations the real
 252 and the imaginary parts of the complex refractive index m ($m=n-ik$, where n is the real part and k is
 253 the imaginary part) were varied in the wide range 1.42–1.56 and 0.001–0.025*i* for dust (Di Biagio et
 254 al., 2017), and 1.50–1.72 and 0.001–0.1*i* for ambient air (Di Biagio et al., 2016), while the value of
 255 1.56-0.001*i* was assumed for kaolinite (Egan and Hilgeman, 1979; Utry et al., 2015). Then, n and k
 256 were set to the values which reproduced the measured β_{sca} at 7-170°. The truncation correction factor
 257 (C_{trunc}) was estimated as the ratio of the modelled β_{sca} at 0°-180° and 7°-170°. At the three
 258 nephelometer wavelengths (450, 550, and 700 nm) the correction factor C_{trunc} varied in the range
 259 1.03-1.06 for ammonium sulfate, 1.08-1.6 for dust, 1.03-1.05 for kaolinite, and 1.05-1.25 for ambient
 260 air. For both approaches (Anderson and Ogren (1998) correction and Mie calculations) the
 261 uncertainty on the truncation correction was estimated to be less than 3%. Once corrected for
 262 truncation, the spectral β_{sca} was used to calculate the scattering Ångström exponent (α_s), which was
 263 then applied to extrapolate β_{sca} at 630 and 660 nm.

264 3.4.3. Determination of the single scattering albedo (SSA)

265 The aerosol single scattering albedo (SSA) represents the ratio of scattering to extinction. At 450 nm,
 266 the SSA was estimated by nephelometer and CAPS data (Eq. 10), while at 660 nm CAPS data were
 267 combined with MAAP observations (Eq. 11):

$$268 \quad \text{SSA}(450) = \frac{\beta_{\text{sca}}(450)_{\text{nephelometer}}}{\beta_{\text{ext}}(450)_{\text{CAPS}}} \quad (10)$$

$$269 \quad \text{SSA}(660) = \frac{\beta_{\text{ext}}(660)_{\text{CAPS}} - \beta_{\text{abs-MAAP}}(660)}{\beta_{\text{ext}}(660)_{\text{CAPS}}} \quad (11)$$

270

271 3.5. Number size distribution and effective fine and coarse diameter

272 The number size distribution was measured by a combination of SMPS and OPC observations. For
 273 the SMPS, corrections for particle loss by diffusion in the instrument tubing and the contribution of
 274 multiple-charged particles were performed using the SMPS software. The electrical mobility diameter
 275 measured by the SMPS can be converted to a geometrical diameter (D_g) by taking into account the
 276 particle dynamic shape factor (χ ; $D_g = D_m/\chi$). In this study, the SMPS showed a good agreement with
 277 OPC data for a shape factor $\chi=1$, which corresponds to spherical particles.

278 The OPC optical-equivalent nominal diameters were converted into sphere-equivalent geometrical
 279 diameters (D_g) by taking into account the aerosol complex refractive index. This consisted in
 280 recalculating the OPC calibration curve for different complex refractive index values. For dust

281 aerosols the refractive index was varied in the range 1.47-1.53 (n) and 0.001-0.005i (k) following the
 282 literature (see Di Biagio et al., 2017) and D_g was set at the mean \pm one standard deviation of the
 283 values obtained for the different n and k. For kaolinite the OPC diameter conversion was performed
 284 by setting the refractive index at 1.56-0.001i. For ambient air the refractive index was set at 1.60-
 285 0.01i, a value that represents a medium absorbing urban polluted aerosol (see Di Biagio et al., 2016).
 286 The impact of humidity on the refractive index of ambient aerosols and associated changes OPC
 287 response were not taken into account. The relative humidity was always below 35% during ambient
 288 air measurements, which implies a very small particle growth. After conversion, the OPC diameter
 289 range became 0.28-18.0 μm for dust (taking into account the particle cut at $\sim 20 \mu\text{m}$ due to the use of
 290 the impactor), and 0.27-58.0 μm for kaolinite and 0.28-65.1 μm for ambient air (the impactor was not
 291 used in these cases). The uncertainty was $<15\%$ at all diameters.

292 The aerosol effective fine ($D_{\text{eff},\text{fine}}$) and coarse ($D_{\text{eff},\text{coarse}}$) diameter were estimated from OPC data as

$$293 \quad D_{\text{eff}} = \frac{\int_{D_1}^{D_2} D_g^3 \frac{dN}{d\log D_g} d\log D_g}{\int_{D_1}^{D_2} D_g^2 \frac{dN}{d\log D_g} d\log D_g} \quad (12)$$

294 with $D_1=0.3 \mu\text{m}$ and $D_2=1 \mu\text{m}$ for the fine mode and $D_1=1 \mu\text{m}$ and $D_2=10 \mu\text{m}$ for the coarse mode.

295 3.6. Data integration and error analysis

296 Aethalometer data were first processed at 2-min resolution to obtain the time evolution of the
 297 attenuation coefficients β_{ATT} and β_{ATT}/R . Data from the MAAP, CAPS, nephelometer, OPC and SMPS
 298 were averaged over 2-min to report them to the same resolution of the aethalometer.

299 Then the β_{ATT} and β_{ATT}/R were calculated over the whole duration of each experiment from Eq. (1)
 300 and (6). Corresponding averages of the reference absorption coefficient ($\beta_{\text{abs-ref}}$) were calculated for
 301 each experiment and used to estimate C_{ref} . Experiment-averages of SSA, $D_{\text{eff},\text{fine}}$, and $D_{\text{eff},\text{coarse}}$ were
 302 also calculated to relate to the obtained C_{ref} .

303 The uncertainty of C_{ref} was estimated with the error propagation formula by taking into account the
 304 uncertainties on β_{ATT} , β_{ATT}/R , and the standard deviation of the averaged $\beta_{\text{abs-ref}}$ from the CAPS-
 305 nephelometer and the MAAP. The uncertainty of β_{ATT} was estimated as the quadratic combination of
 306 the uncertainty of the linear fit of ΔATT with respect to time and the uncertainties on the surface
 307 deposit A. The uncertainty of β_{ATT}/R was estimated taking into account the uncertainty of β_{ATT} and R.
 308 Uncertainties on β_{ATT} and β_{ATT}/R are both $\sim 20\%$.

309 4. Results

310 The time series of observations for all the experiments are shown in **Fig. 2** as 2-min averages. Seven
 311 experiments were performed on mineral dust issued from six different areas in the Sahel (Niger),
 312 Eastern Asia (China), North America (Arizona), Northern Africa (Tunisia), Australia, and Southern
 313 Africa (Namibia), and on a kaolinite powder. Experiments were performed between the 3rd and the 9th
 314 of November 2016 and lasted between 1 and 2 hours each. The experiment on Niger dust (labelled
 315 as Niger 1 and Niger 2) were duplicated to test the repeatability of the obtained C_{ref} . Ambient air data

316 were collected between the 8th and the 14th November 2016 for a total of 7 hours of measurements.
317 Eight different periods characterized by little variation and different levels of SSA were selected in the
318 whole set of ambient air measurements. These are identified as ambient air 1 to 8. The summary of
319 information is provided in **Table 2**. SMPS data were available for ammonium sulfate and kaolinite
320 experiments, for one of the two Niger dust experiments (Niger 2), and for some of the ambient air
321 experiments. OPC measurements were performed for all experiments with the exception of the
322 ammonium sulfate.

323 **4.1. Quality control data**

324 Results of the ammonium sulfate control experiment (24 October 2016), used to test the performance
325 of the optical instruments, are illustrated in **Fig. 3**. As expected for this purely scattering aerosol (Toon
326 et al., 1976), the nephelometer scattering and the CAPS extinction at 450 and 630 nm were in very
327 good agreement (less than 4% difference) during the whole duration of the experiment. This is well
328 below the single instrument uncertainty of $\pm 9\%$ for the nephelometer (Sherman et al., 2015) and $\pm 5\%$
329 for the CAPS (Massoli et al., 2010). This is further demonstrated by the scatterplot of their respective
330 10-minute averages, yielding a linear regression in the form of $y=0.95x+5.1$ ($R^2=0.95$) at 450 nm and
331 $y=1.01x-1.4$ ($R^2=0.98$) at 630 nm. The average β_{ext} at 450 and 630 nm from CAPS observations was
332 $913 (\pm 52)$ and $424 (\pm 33)$ Mm^{-1} , respectively, while the average β_{sca} was $921 (\pm 36)$ and $420 (\pm 17)$.
333 This led to an average SSA of $1.01 (\pm 0.07)$ at 450 nm and $0.99 (\pm 0.07)$ at 630 nm.

334 The absorption coefficient, averaged over the duration of the experiment, was $0.10 (\pm 0.04)$ Mm^{-1} at
335 450 nm and $0.24 (\pm 0.07)$ Mm^{-1} at 660 nm according to the aethalometer, and $0.82 (\pm 0.13)$ Mm^{-1} at
336 660 nm according to the MAAP. For the aethalometer, the absorption coefficient was calculated from
337 Eq. (2) assuming $C_{\text{ref}}=2.14$ and the R formulation by C2010 (Eq. 6b). The $\alpha(\lambda)$ coefficient was
338 calculated from Eq. (3). The c and d terms in Eq. (3) were determined from the power-law fit of $\beta_{\text{ATT}}(\lambda)$
339 vs $\beta_{\text{sca}}(\lambda)$ and are $c=(0.56 \pm 0.06)$ Mm^{-1} and $d=(0.485 \pm 0.09)$. These values are lower than those
340 reported by Arnott et al. (2005) ($c=0.797$, $d=0.564$). The A and α_S terms, obtained from the power law
341 fit of $\beta_{\text{sca}}(\lambda)$ vs wavelength (Eq. 3) are $A=(4.07 \pm 0.49)10^9$ Mm^{-1} and $\alpha_S=(-2.46 \pm 0.12)$.

342 **Figure 4** shows the extinction coefficient at 660 nm extrapolated from CAPS observations and
343 calculated as the sum of nephelometer and MAAP data for dust, kaolinite, and ambient air
344 experiments. The linear regression of the data yields $y=1.03x-0.5$ ($R^2=0.99$), indicating the
345 consistency of optical measurements between the CAPS, nephelometer, and MAAP (less than 3%
346 difference on average). Based on the success of the optical closure at 660 nm, we therefore assume
347 the “CAPS minus nephelometer” approach appropriate to estimate the aerosol absorption coefficient
348 at 450 nm.

349 **4.2. Estimate of C_{ref}**

350 The C_{ref}^* , $C_{\text{ref}}(\text{W2003})$ and $C_{\text{ref}}(\text{C2010})$ at 450 and 660 nm obtained for all different experiments and
351 the corresponding aerosol SSA, $D_{\text{eff, fine}}$, and $D_{\text{eff, coarse}}$ are summarized in **Table 2**.

352 C_{ref} for mineral dust varied between 1.81 and 2.56 for a SSA of 0.85–0.96 at 450 nm and between
353 1.75 and 2.28 for a SSA of 0.98–0.99 at 660 nm. The estimate for Niger 1 and 2 samples agreed

354 within 4.9%, which suggests a good repeatability of the C_{ref} estimate. For kaolinite C_{ref} was 2.47–2.51
355 and 2.31–2.34 at 450 and 660 nm, respectively, with an associated SSA of 0.96 and 0.97 at the two
356 wavelengths. For ambient air C_{ref} varied in the range 1.91–4.35 for a SSA of 0.62–0.87 at 450 nm and
357 1.66–2.96 for and SSA of 0.42–0.76 at 660 nm. For samples 6 and 8 the C_{ref} at 450 was lower than at
358 660 nm. Otherwise, for all other cases, the C_{ref} was larger at 450 nm than at 660 nm.

359 Differences within 2.8% were obtained between C_{ref}^* , $C_{ref}(W2003)$ and $C_{ref}(C2010)$ at 450 and 660 nm
360 for weakly-absorbing dust and kaolinite. In contrast, for more absorbing ambient air aerosols the
361 differences between C_{ref}^* , $C_{ref}(W2003)$ and $C_{ref}(C2010)$ were in the range 2.7% to 24.3%. The different
362 ATT threshold assumed here (20%) compared to W2003 and C2010 (10%) has a negligible impact
363 (less than 1% difference) on the results. In some cases (ambient air 1–2 and Niger 1 samples),
364 however, we obtained $C_{ref}(C2010) > C_{ref}(W2003)$; these cases correspond to a mean aethalometer
365 measured $ATT < 10\%$, for which $R(W2003) > R(C2010)$, and this explains the larger $C_{ref}(C2010)$.
366 Conversely, $C_{ref}(C2010) < C_{ref}(W2003)$ when the measured ATT was $\sim 15\text{--}20\%$, yielding
367 $R(W2003) < R(C2010)$. The percent difference between the obtained $C_{ref}(W2003)$ and $C_{ref}(C2010)$
368 increased for decreasing SSA due to the increase of the $R(W2003)$ to $R(C2010)$ absolute difference
369 for decreasing SSA. When averaging data for all ambient air samples, the two formulations yield very
370 similar values. For example, at 660 nm the mean $C_{ref}(W2003)$ was 2.44 (± 0.38), less than 2% larger
371 than the mean $C_{ref}(C2010)$ of 2.39 (± 0.35).

372 The mean and standard deviation of the multiple scattering correction at 450 and 660 nm for dust,
373 kaolinite, and ambient air calculated as the mean of the C_{ref}^* , $C_{ref}(W2003)$, and $C_{ref}(C2010)$ are
374 reported in **Table 3**. The mean C_{ref} at 450 and 660 nm is 2.09 (± 0.22) and 1.92 (± 0.17) for dust, 2.49
375 (± 0.02) and 2.31 (± 0.02) for kaolinite, and 2.32 (± 0.36) and 2.32 (± 0.35) for pollution aerosols. If the
376 wavelength of 637 nm is assumed for the MAAP instead of 670 nm, as suggested by Müller et al.
377 (2011), the average C_{ref} at 660 nm would increase by up to $\sim 15\%$ for dust and ambient air (2.17 \pm 0.19
378 and 2.48 \pm 0.41, respectively) and $\sim 3\%$ for kaolinite (2.40 \pm 0.02).

379 **4.3. Dependence of C_{ref} on SSA**

380 As reported in Table 2, very different SSA values at 450 and 660 nm were obtained for the various
381 cases. For dust aerosols, the measured SSA values were larger than 0.85 at 450 nm and close to
382 unity (>0.98) at 660 nm, in line with field observations of dust from different sources (Schladitz et al.,
383 2009; Formenti et al., 2011; Ryder et al., 2013). In particular, our results for China, Arizona, and
384 Australia samples are in line with published values by Engelbrecht et al. (2016), who used a
385 photoacoustic instrument to measure absorption of re-suspended dust aerosols. This would suggest
386 the similar performances of the aethalometer compared to the photoacoustic technique. The SSA for
387 kaolinite was 0.96–0.97 at 450 and 660 nm, in agreement with Utry et al. (2017) also using a
388 photoacoustic method to measure absorption (0.97 and 0.99 (± 0.04) at 450 and 635 nm, respectively).
389 Both at 450 and 660 nm, the single scattering albedo for ambient air varied in the wide range 0.2 to
390 0.9 during the whole measurement period (see Fig. 2 for measurements at 660 nm). The average
391 values obtained for air samples 1–8 were 0.62–0.87 at 450 and 0.42–0.76 at 660 nm. The SSA
392 decreased with increasing wavelength, as expected for pollution aerosols (e.g., Bergstrom et al.,

393 2007; Di Biagio et al., 2016). The wide range of values indicates the occurrence of particles with very
394 different absorption properties, henceforth chemical composition (or complex refractive index) and/or
395 different size distribution (e.g., Moosmüller and Arnott, 2009). For instance, in urban environments,
396 Bergstrom et al. (2007) reported SSA in the range 0.2–1.0 at 550 nm, with lowest values observed for
397 soot-dominated air masses and highest values for urban pollution dominated by low-absorbing
398 organic components.

399 The experimental SSA values serve two purposes. First, as shown in **Fig. 5**, they are linearly related
400 to the factor f in the loading effect correction term R in Eq. (6a)-(6b) as $f=a(1-SSA)+1$. The linear
401 regression of our data yields a slope $a=(1.48 \pm 0.14)$, larger than the value of 0.85 reported in W2003
402 (f data from W2003 are also shown in Fig. 5) and 0.76 in C2010.

403 Secondly, SSA data serve to investigate the dependence of C_{ref} on relative amounts of particle
404 absorption for mineral dust. As shown in **Fig. 6** (top panel), C_{ref} for dust seems to be independent of
405 SSA at 660 nm, whereas it decreases for increasing SSA at 450 nm. This trend is statistically
406 significant (correlation coefficient of $R^2=0.85$). The relationship between C_{ref} and SSA is also
407 investigated in **Fig. 6** (bottom panel) for all aerosol samples. Globally, Fig. 6 suggests a decrease of
408 C_{ref} for increasing SSA, in particular at 450 nm, albeit with a poorer statistical significance at both
409 wavelengths ($R^2=0.35$ and 0.59). Data are also compared to those reported in W2003 and C2010 at
410 660 nm for different aerosol types. Diesel soot and soot mixed with ammonium sulfate were
411 investigated in W2003, while C2010 reported data for ambient aerosols sampled at different locations
412 in Europe and in Amazonia. W2003 also reported the C_{ref} for soot particles at 450 nm (not shown in
413 Fig. 6), with values between 2.08 and 3.64; these values are in line with our observations at 450 nm
414 for ambient air. Whereas, as illustrated in Fig. 6, both W2003 and C2010 found a relationship
415 between C_{ref} and SSA at 660 nm, contrasting results are obtained when plotting the two datasets
416 together. C2010 obtained a sharp and almost linear decrease of C_{ref} with increasing SSA ($C_{ref}\sim 5-2.5$
417 for $SSA\sim 0.65-0.9$), while W2003 data showed a pronounced decrease of C_{ref} ($\sim 2-4$) for increasing
418 SSA in the range 0.5 and 0.7 and low C_{ref} values (~ 2) at $SSA\sim 0.2$. Our data for dust and kaolinite at
419 high SSA (>0.97) seem to follow the same linear relationship as C2010. However at lower SSA, our
420 data for ambient aerosols are closer to W2003 results at 660 nm. These differences between W2003
421 and C2010 data, and also with our results, are quite difficult to explain. The main difference between
422 W2003 compared to C2010 is that W2003 performed measurements in a simulation chamber, while
423 C2010 was a field study. Working in ambient conditions may influence the retrieved C_{ref} . In fact,
424 volatile-organic compounds or water vapor present in the atmosphere may condense on the filter
425 (Lack et al., 2008), thus enhancing the scattering from the filter fibers and leading to higher C_{ref} . This
426 could explain the higher C_{ref} obtained in C2010 compared to W2003. Our results for ambient air
427 particles, however, are in agreement with W2003 chamber results. Differences in the size distributions
428 of the investigated aerosols are also expected to possibly affect the comparison; however, no detailed
429 information on the size of investigated aerosols is provided in W2003 and C2010. Another source of
430 discrepancy may be in the fact that, differently from W2003 and our study, where aethalometer and
431 MAAP were compared at 660 nm, C_{ref} in C2010 was estimated by comparing aethalometer data at

432 660 nm with MAAP observations at 630 nm. As aerosol absorption increases with decreasing
433 wavelength, this wavelength difference may induce an underestimation of C_{ref} in C2010.

434 **4.4. Dependence of C_{ref} on particles size**

435 Examples of the number size distribution measured by the SMPS and OPC for ammonium sulfate,
436 Niger dust, kaolinite, and ambient air are shown in **Fig. 7**. Ammonium sulfate had mostly a submicron
437 distribution, while dust aerosols presented the largest fraction over the whole super-micron range up
438 to about 10-20 μm . Dust particles larger than 20 μm were completely suppressed by the impactor
439 system and were not detected by the OPC. The coarse component, up to about 10 μm , was also
440 identified in the kaolinite and ambient air samples. In particular, a defined mode at ~ 4 μm was
441 detected in the number distribution of ambient air particles, and may be linked to the presence of
442 soot-aggregates, tire abrasions, re-suspended road dust, or bioaerosols (Harrison et al., 2001; Bauer
443 et al., 2008; Pakbin et al., 2010; Liu and Harrison, 2011). The $D_{eff, fine}$ varied between 0.24 and 0.62
444 μm and the $D_{eff, coarse}$ between 2.3 and 6.2 μm for the different cases (Table 2). For mineral dust,
445 $D_{eff, coarse}$ ranged between 2.3 and 3.6 μm , encompassing the value of $D_{eff, coarse} \sim 3$ μm reported by
446 Denjean et al. (2016b) in their figure 11 for Saharan dust both close to sources and during transport
447 over the Atlantic.

448 These observations are consistent with the extinction (α_E) and the absorption (α_A) Ångstrom exponent
449 measured during the experiments. The α_E (shown in Fig.2) was ~ 0 for kaolinite, varied between about
450 0 and 2 for mineral dust aerosols, and between 0.5 and 2.5 for ambient air, indicating particles with
451 variable sizes, both the sub-micron and the super-micron fractions. The absorption Ångström
452 coefficient α_A obtained from aethalometer data was between 2.2 and 4 for dust, between 1 and 1.5 for
453 kaolinite and between 0.5 and 1.5 for ambient air aerosols.

454 The dependence of C_{ref} at 450 and 660 nm on the effective diameter fine $D_{eff, fine}$ and coarse $D_{eff, coarse}$
455 as a measure of particle size was investigated. The scatterplot of C_{ref} versus $D_{eff, coarse}$ is shown in **Fig.**
456 **8** and indicates that the C_{ref} does not have any statistically significant dependence on the particle size
457 for mineral dust at both wavelengths and for all data at 660 nm ($R^2 \leq 0.40$). Conversely, a slight
458 increase of C_{ref} for increasing $D_{eff, coarse}$ is obtained at 450 nm when all aerosol samples are considered
459 ($R^2 = 0.70$). In contrast, no dependence of C_{ref} on $D_{eff, fine}$ is found ($R^2 \leq 0.44$, not shown).

460 **5. Conclusions**

461 In this paper we presented an intercomparison study between an aethalometer and a MAAP, a
462 nephelometer, and two CAPS with the aim of determining a two-wavelength multiple scattering
463 correction (C_{ref}) for aethalometer measurements for weakly-absorbing mineral dust aerosols. Mineral
464 dust aerosols investigated here were generated from natural parent soils collected in desert areas,
465 both in the Northern and in the Southern hemisphere (Di Biagio et al., 2014; 2017). The size
466 distribution of the generated dust included both the submicron and the supermicron fractions, with an
467 effective fine and coarse diameter between 0.32–0.55 and 2.3–3.6 μm , respectively.

468 The estimated C_{ref} was in the range 1.81–2.56 at 450 nm and 1.75–2.28 at 660 nm for the different
469 dust samples, with mean C_{ref} values of 2.09 (± 0.22) and 1.92 (± 0.17), respectively. Using these

470 values of C_{ref} , the dust absorption coefficient estimated by the aethalometer will be about 2% (450
471 nm) and 11% (660 nm) higher than obtained by using the wavelength-independent value of 2.14,
472 commonly used in the literature (e.g., Sandradewi et al., 2008; Formenti et al., 2011; Di Biagio 2016).
473 The new estimate of C_{ref} has a negligible impact on the dust SSA at 450 nm (less than 0.5%
474 difference between the value obtained for $C_{ref}=2.09$ or 2.14), but affects by up to ~3% the estimate of
475 SSA at 660 nm.

476 Given that the median of the solar spectrum occurs at about 700 nm, the expected change in the dust
477 SSA at 660 nm may significantly affect the impact of dust on radiation. Mallet et al. (2009) estimated
478 that about a 3% change in the visible SSA of dust may determine up to a 10% change in the radiative
479 effect of dust at the surface, and up to 20% change at the Top of the Atmosphere, with a net ~25%
480 increase of dust absorption in the atmosphere. Given the strong sensitivity of the dust direct effect to
481 particle absorption (Solmon et al., 2008; Mallet et al., 2009; Di Biagio et al., 2010; Jin et al., 2016,
482 among others), we recommend this new C_{ref} value at 660 nm to be used when analyzing
483 aethalometer data for mineral dust aerosols.

484 The analysis performed in this study indicates that there is no dependence of C_{ref} on the coarse
485 component of the particle size distribution for dust. This suggests that the C_{ref} obtained here can be
486 used to correct aethalometer data for dust at emission, when the coarse fraction dominates the dust
487 size distribution, as well as after long-range transport, when the coarsest component of dust has
488 preferentially settled out.

489 Finally, our body of observations, spanning a wide range of SSA values from 0.96–0.97 (kaolinite) to
490 ~0.4–0.8 (ambient urban aerosols), indicates that C_{ref} decreases for increasing SSA, both at 450 and
491 660 nm. This is generally consistent with the results of W2003 and C2010 at 660 nm. However, a
492 unique relationship cannot be established. At high SSA (>0.90), our data, as well as those of C2010,
493 suggest a sharper decrease than at SSA in the range 0.4-0.8, where our data are more consistent
494 with those of W2003. Differences in aerosol sampling conditions and in the exact analysed
495 wavelengths from the three studies may be the cause of such discrepancy, but clear conclusions, as
496 well as an explicit relationship between C_{ref} and SSA, are still difficult to give. Similarly, our
497 observations seem to indicate that C_{ref} increases for increasing $D_{eff,coarse}$ at 450 nm. This trend was
498 only observed when the entire dataset was considered, but not if the dataset was limited to just the
499 dust observations, making it difficult to draw clear conclusions.

500 A more extensive characterization of C_{ref} is required to provide an appropriate correction of
501 aethalometer data under the wide range of atmospheric conditions.

502 **Data availability**

503 Experimental and processed data are available upon request to the contact author.

504 **Author contributions**

505 C. Di Biagio and P. Formenti designed the experiments, discussed the results, and wrote the
506 manuscript with comments from all co-authors. N. Marchand provided the MAAP used in the

507 experiments. C. Di Biagio, M. Cazaunau, and E. Pangui performed the experiments. C. Di Biagio
508 performed the data analysis.

509 **Competing interests**

510 The authors declare that they have no conflict of interest.

511 **Acknowledgements**

512 The RED-DUST project was supported by the French national programme LEFE/INSU, by the Institut
513 Pierre Simon Laplace (IPSL), and by OSU-EFLUVE (Observatoire des Sciences de l'Univers-
514 Enveloppes Fluides de la Ville à l'Exobiologie) through dedicated research funding. C. Di Biagio was
515 supported by the CNRS via the Labex L-IPSL, which is funded by the ANR (grant no. ANR-10-LABX-
516 0018). This work has also received funding from the European Union's Horizon 2020 (H2020)
517 research and innovation programme through the EUROCHAMP-2020 Infrastructure Activity under
518 grant agreement No 730997. The authors thank K. Kandler, D. Seibert, and the LISA staff who
519 collected the soil samples used in this study, E. Journet who provided the kaolinite sample, A. Petzold
520 for helpful discussions on the aethalometer multiple scattering effects, and B. Tamime-Roussel for
521 logistic help with the MAAP. The three anonymous reviewers are also gratefully acknowledged for
522 their helpful comments which allowed improving and clarifying the manuscript.

523

524 **References**

525 Anderson, T. L. and Ogren, J. A.: Determining aerosol radiative properties using the TSI 3563
526 integrating nephelometer, *Aerosol Sci. Technol.*, 29, 57–69, 1998.

527 Andreae, M. O. and Gelencsér, A.: Black Carbon or Brown Carbon? The Nature of Light-Absorbing
528 Carbonaceous Aerosols. *Atmos. Chem. Phys.* 6:3131–3148, 2006.

529 Arnott, W. P., Hamasha, K., Moosmüller, H., Sheridan, P. J., and Ogren, J. A.: Towards aerosol
530 light-absorption measurements with a 7-wavelength aethalometer: Evaluation with a photoacoustic
531 instrument and 3-wavelength nephelometer, *Aerosol Sci. Tech.*, 39, 17–29, 2005.

532 Backman, J., Schmeisser, L., Virkkula, A., Ogren, J. A., Asmi, E., Starkweather, S., Sharma, S.,
533 Eleftheriadis, K., Uttal, T., Jefferson, A., Bergin, M., and Makshtas, A.: On Aethalometer
534 measurement uncertainties and multiple scattering enhancement in the Arctic, *Atmos. Meas. Tech.*
535 Discuss., doi:10.5194/amt-2016-294, in review, 2016.

536 Balkanski, Y., Schulz, M., Claquin, T., and Guibert, S.: Reevaluation of Mineral aerosol radiative
537 forcings suggests a better agreement with satellite and AERONET data, *Atmos. Chem. Phys.*, 7,
538 81–95, doi:10.5194/acp-7-81-2007, 2007.

539 Bauer, H., Schueller, E., Weinke, G., Berger, A., Hitenberger, R., Marr, I. L., and Puxbaum, H.:
540 Significant contributions of fungal spores to the organic carbon and to the aerosol mass balance of
541 the urban atmospheric aerosol, *Atmos. Environ.*, 42, 5542-5549, 2008.

542 Bergstrom, R. W., Pilewskie, P., Russell, P. B., Redemann, J., Bond, T. C., Quinn, P. K., and Sierau,
543 B.: Spectral absorption properties of atmospheric aerosols, *Atmos. Chem. Phys.*, 7, 5937-5943,
544 doi:10.5194/acp-7-5937-2007, 2007.

545 Caponi, L., Formenti, P., Massabó, D., Di Biagio, C., Cazaunau, M., Pangui, E., Chavaille, S.,
546 Landrot, G., Fonda, E., Andreae, M. O., Kandler, K., Piketh, S., Saeed, T., Seibert, D., Williams, E.,
547 Balkanski, Y., Prati, P., and Doussin, J.-F.: Spectral- and size-resolved shortwave mass absorption
548 cross-sections of mineral dust aerosols: a smog chamber study, *Atmos. Chem. Phys.*, 17, 7175-
549 7191, <https://doi.org/10.5194/acp-17-7175-2017>, 2017.

550 Cattrall, C., Carder, K. L., and Gordon, H. R.: Columnar aerosol single-scattering albedo and phase
551 function retrieved from sky radiance over the ocean: measurements of Saharan dust, *J. Geophys.*
552 *Res.*, 108(D9), 4287, doi:10.1029/2002JD002497, 2003.

553 Collaud Coen, M., Weingartner, E., Apituley, A., Ceburnis, D., Fierz-Schmidhauser, R., Flentje, H.,
554 Henzing, J. S., Jennings, S. G., Moerman, M., Petzold, A., Schmid, O., and Baltensperger, U.:
555 Minimizing light absorption measurement artifacts of the Aethalometer: evaluation of five correction
556 algorithms, *Atmos. Meas. Tech.*, 3, 457–474, doi:10.5194/amt-3-457-2010, 2010.

557 DeCarlo, P., Worsnop, D. R., Slowik, J. G., Davidovits, P., and Jimenez, J. L.: Particle Morphology
558 and Density Characterization by Combined Mobility and Aerodynamic Diameter Measurements. Part
559 1: Theory, *Aerosol Sci. Technol.*, 38(12), 1185-1205, 2004.

560 Denjean, C., Formenti, P., Desboeufs, K., Chevaillier, S., Triquet, S., Maillé, M., Cazaunau, M.,
561 Laurent, B., Mayol-Bracero, O. L., Vallejo, P., Quiñones, M., Gutierrez-Molina, I. E., Cassola, F.,
562 Prati, P., Andrews, E., and Ogren, J.: Size distribution and optical properties of African mineral dust
563 after intercontinental transport, *J. Geophys. Res. Atmos.*, 121, 7117–7138,
564 doi:10.1002/2016JD024783, 2016a.

565 Denjean, C., Cassola, F., Mazzino, A., Triquet, S., Chevaillier, S., Grand, N., Bourriane, T.,
566 Mombosse, G., Sellegri, K., Schwarzenbock, A., Freney, E., Mallet, M., and Formenti, P.: Size
567 distribution and optical properties of mineral dust aerosols transported in the western Mediterranean,
568 *Atmos. Chem. Phys.*, 16, 1081-1104, doi:10.5194/acp-16-1081-2016, 2016b.

569 Di Biagio, C., di Sarra, A., and Meloni, D.: Large atmospheric shortwave radiative forcing by
570 Mediterranean aerosols derived from simultaneous ground-based and spaceborne observations and
571 dependence on the aerosol type and single scattering albedo, *J. Geophys. Res.*, 115, D10209, doi:
572 10.1029/2009JD012697, 2010.

573 Di Biagio, C., Formenti, P., Styler, S. A., Pangui, E., and Doussin, J.-F.: Laboratory chamber
574 measurements of the longwave extinction spectra and complex refractive indices of African and
575 Asian mineral dusts, *Geophys. Res. Lett.*, 41, 6289-6297, doi:10.1002/2014GL060213, 2014.

576 Di Biagio, C., Formenti, P., Doppler, L., Gaimoz, C., Grand, N., Ancellet, G., Attié, J.-L., Bucci, S.,
577 Dubuisson, P., Fierli, F., Mallet, M., and Ravetta, F.: Continental pollution in the Western
578 Mediterranean basin: large variability of the aerosol single scattering albedo and influence on the
579 direct shortwave radiative effect, *Atmos. Chem. Phys.*, 16, 10591-10607, doi:10.5194/acp-16-10591-
580 2016, 2016.

581 Di Biagio, C., Formenti, P., Balkanski, Y., Caponi, L., Cazaunau, M., Pangui, E., Journet, E., Nowak,
582 S., Caquineau, S., Andreae, M. O., Kandler, K., Saeed, T., Piketh, S., Seibert, D., Williams, E., and
583 Doussin, J.-F.: Global scale variability of the mineral dust longwave refractive index: a new dataset
584 of in situ measurements for climate modelling and remote sensing, *Atmos. Chem. Phys.*, 17, 1901-
585 1929, doi:10.5194/acp-17-1901-2017, 2017.

586 di Sarra, A., C. Di Biagio, D. Meloni, F. Monteleone, G. Pace, S. Pugnaghi, and D. Sferlazzo,
587 Shortwave and longwave radiative effects of the intense Saharan dust event of March 25-26, 2010,
588 at Lampedusa (Mediterranean sea), *J. Geophys. Res.*, 116, D23209, doi:10.1029/2011JD016238,
589 2011.

590 Egan, W. G. and Hilgeman, T. W.: *Optical Properties of Inhomogeneous Materials: Applications to*
591 *Geology, Astronomy, Chemistry, and Engineering*, Academic Press, 235 pp, 1979.

592 Engelbrecht, J. P., Moosmüller, H., Pincock, S., Jayanty, R. K. M., Lersch, T., and Casuccio, G.:
593 Technical note: Mineralogical, chemical, morphological, and optical interrelationships of mineral dust
594 re-suspensions, *Atmos. Chem. Phys.*, 16, 10809-10830, doi:10.5194/acp-16-10809-2016, 2016.

595 Fialho, P., Hansen, A. D. A., and Honrath, R. E.: Absorption coefficients by aerosols in remote
596 areas: a new approach to decouple dust and black carbon absorption coefficients using seven-
597 wavelength Aethalometer data, *Aerosol Sci.*, 36, 267–282, 2005.

598 Formenti, P., Rajot, J. L., Desboeufs, K., Said, F., Grand, N., Chevaillier, S., and Schmechtig, C.:
599 Airborne observations of mineral dust over western Africa in the summer Monsoon season: spatial
600 and vertical variability of physico-chemical and optical properties, *Atmos. Chem. Phys.*, 11, 6387-
601 6410, doi:10.5194/acp-11-6387-2011, 2011.

602 Goudie A. S., and Middleton, N. J.: *Desert dust in the global system*. Springer, Berlin, Heidelberg,

603 New York, 2006.

604 Hansen, A. D. A., Rosen, H., and Novakov, T.: The aethalometer—an instrument for the real-time
605 measurement of optical absorption by aerosol particles. *The Science of the Total Environment*, 36,
606 191–196, 1984.

607 Harrison, R. M., Yin, J., Mark, D., Stedman, J., Appleby, R.S., Booker, J., and Moorcroft, S.: Studies
608 of the coarse particle (2.5–10 μm) component in UK urban atmospheres, *Atmos. Environ.*, 35,
609 3667–3679, 2001.

610 Heim, M., Mullins, B. J., Umhauer, H., and Kasper, G.: Performance evaluation of three optical
611 particle counters with an efficient “multimodal” calibration method, *J. Aerosol Sci.*, 39, 1019–1031,
612 2008.

613 Heinold, B., I. Tegen, K. Schepanski, and O. Hellmuth, Dust radiative feedback on Saharan boundary
614 layer dynamics and dust mobilization, *Geophys. Res. Lett.*, 35, L20817,
615 doi:10.1029/2008GL035319, 2008.

616 Highwood, E. J. and Ryder, C. L.: Radiative Effects of Dust, in: *Mineral Dust: A Key Player in the*
617 *Earth System*, edited by: Knippertz, P. and Stuut, J.-B. W., Springer ScienceCBusiness Media,
618 Dordrecht, https://doi.org/10.1007/978-94-017-8978-3_11, 2014.

619 Horvath, H.: Atmospheric Light Absorption - A Review, *Atmos. Environ.*, 27A(3), 293-317, 1993.

620 Jin, Q., Zang, Z.-L., and Wei, J.: High sensitivity of Indian summer monsoon to Middle East dust
621 absorptive properties, *Sci. Rep.*, 6:30690, doi: 10.1038/srep30690, 2016.

622 Kandler, K., Schütz, L., Deutscher, C., Ebert, M., Hofmann, H., Jäckel, S., Jaenicke, R., Knippertz, P.,
623 Lieke, K., Massling, A., Petzold, A., Schladitz, A., Weinzierl, B., Wiedensohler, A., Zorn, S., and
624 Weinbruch, S.: Size distribution, mass concentration, chemical and mineralogical composition and
625 derived optical parameters of the boundary layer aerosol at Tinfou, Morocco, during SAMUM 2006,
626 *Tellus B*, 61, 32–50, doi:10.1111/j.1600-0889.2008.00385.x, 2009.

627 Lack, D. A., Cappa, C. D., Covert, D. S., Baynard, T., Massoli, P., Sierau, B., Bates, T. S., Quinn, P.
628 K., Lovejoy, E. R., and Ravishankara, A. R.: Bias in Filter-Based Aerosol Light Absorption
629 Measurements Due to Organic Aerosol Loading: Evidence from Ambient Measurements, *Aerosol*
630 *Sci. Tech.*, 42, 1033-1041, 2008.

631 Liu, X. J., and Harrison, R. M.: Properties of coarse particles in the atmosphere of the United
632 Kingdom, *Atmos. Environ.*, 45, 3267–3276, 2011.

633 Mallet, M., Tulet, P., Serça, D., Solmon, F., Dubovik, O., Pelon, J., Pont, V., and Thouron, O.: Impact
634 of dust aerosols on the radiative budget, surface heat fluxes, heating rate profiles and convective
635 activity over West Africa during March 2006, *Atmos. Chem. Phys.*, 9, 7143-7160, doi:10.5194/acp-9-
636 7143-2009, 2009.

637 Massoli, P., Kebejian, P. L., Onasch, T. B., Hills, F. B., and Freedman, A.: Aerosol Light Extinction
638 Measurements by Cavity Attenuated Phase Shift (CAPS) Spectroscopy: Laboratory Validation and
639 Field Deployment of a Compact Aerosol Particle Extinction Monitor, *Aerosol Sci. Technol.*, 44, 428–
640 435, doi:10.1080/02786821003716599, 2010.

641 Miller, R.L., I. Tegen, and J.P. Perlwitz: Surface radiative forcing by soil dust aerosols and the
642 hydrologic cycle. *J. Geophys. Res.*, 109, D04203, doi:10.1029/2003JD004085, 2004.

643 Miller, R.L., Knippertz, P., Pérez García-Pando, C., Perlwitz, J. P., and Tegen, I.: Impact of dust
644 radiative forcing upon climate. In *Mineral Dust: A Key Player in the Earth System*. P. Knippertz, and
645 J.-B.W. Stuut, Eds. Springer, 327-357, doi:10.1007/978-94-017-8978-3_13, 2014.

646 Moosmüller, H., and Arnott, W. P.: Particle Optics in the Rayleigh Regime, *J. Air & Waste Manage.*
647 *Assoc.*, 59, 1028-1031, 2009.

648 Moosmüller, H., Chakrabarty, R. K., and Arnott, W. P.: Aerosol Light Absorption: A Review, *J. Quant.*
649 *Spectr. Rad. Transf.*, 110(11), 844-878, 2009.

650 Müller, T., Henzing, J. S., de Leeuw, G., Wiedensohler, A., Alastuey, A., Angelov, H., Bizjak, M.,
651 Collaud Coen, M., Engström, J. E., Gruening, C., Hillamo, R., Hoffer, A., Imre, K., Ivanow, P.,
652 Jennings, G., Sun, J. Y., Kalivitis, N., Karlsson, H., Komppula, M., Laj, P., Li, S.-M., Lunder, C.,
653 Marinoni, A., Martins dos Santos, S., Moerman, M., Nowak, A., Ogren, J. A., Petzold, A., Pichon, J.

654 M., Rodriguez, S., Sharma, S., Sheridan, P. J., Teinilä, K., Tuch, T., Viana, M., Virkkula, A.,
655 Weingartner, E., Wilhelm, R., and Wang, Y. Q.: Characterization and intercomparison of aerosol
656 absorption photometers: result of two intercomparison workshops, *Atmos. Meas. Tech.*, 4, 245-268,
657 doi:10.5194/amt-4-245-2011, 2011.

658 Pakbin, P., Hudda, N., Cheng, K. L., Moore, K. F., Sioutas, C.: Spatial and temporal variability of
659 coarse (PM_{10-2.5}) particulate matter concentrations in the Los Angeles area, *Aerosol Sci. Technol.*,
660 44, 514–525, 2010.

661 Perez, C., Nickovic, S., Baldasano, J. M., Sicard, M., Rocadenbosch, F., and Cachorro, V. E.: A long
662 Saharan dust event over the western Mediterranean: Lidar, Sun photometer observations, and
663 regional dust modeling, *J. Geophys. Res.*, 111, D15214, doi:10.1029/2005JD006579, 2006.

664 Petzold, A., and Schönlinner, M.: Multiangle Absorption Photometry—A New Method for the
665 Measurement of Aerosol Light Absorption and Atmospheric Black Carbon, *J. Aerosol Sci.*, 35:421–
666 441, 2004.

667 Petzold, A., Schloesser, H., Sheridan, P. J., Arnott, W. P., Ogren, J. A., and Virkkula, A.: Evaluation of
668 Multi-angle Absorption Photometry for Measuring Aerosol Light Absorption, *Aerosol Sci. Technol.*,
669 39, 40–51, 2005.

670 Querol, X., Pey, J., Pandolfi, M., Alastuey, A., Cusack, M., Pérez, N., Moreno, T., Viana, M.,
671 Mihalopoulos, N., Kallos, G., and Kleanthous, S.: African dust contributions to mean ambient PM10
672 mass-levels across the Mediterranean Basin, *Atmos. Environ.*, 43, 4266-4277, 2009.

673 Reddy, M. S., O. Boucher, Y. Balkanski, and M. Schulz: Aerosol optical depths and direct radiative
674 perturbations by species and source type. *Geophys. Res. Lett.*, 32, L12803, 2005.

675 Redmond, H. E., Dial, K. D., and Thompson, J. E.: Light scattering and absorption by wind blown
676 dust: Theory, measurement, and recent data, *Aeolian Res.*, 2, 5–26, 2010.

677 Ryder, C. L., Highwood, E. J., Rosenberg, P. D., Trembath, J., Brooke, J. K., Bart, M., Dean, A.,
678 Crosier, J., Dorsey, J., Brindley, H., Banks, J., Marsham, J. H., McQuaid, J. B., Sodemann, H., and
679 Washington, R.: Optical properties of Saharan dust aerosol and contribution from the coarse mode
680 as measured during the Fennec 2011 aircraft campaign, *Atmos. Chem. Phys.*, 13, 303-325,
681 doi:10.5194/acp-13-303-2013, 2013.

682 Sandradewi, J., Prévôt, A. S. H., Weingartner, E., Schmidhauser, R., Gysel, M., and Baltensperger,
683 U.: A study of wood burning and traffic aerosols in an Alpine valley using a multi-wavelength
684 Aethalometer, *Atmos. Environ.*, 42, 101-112, 2008.

685 Saturno, J., Pöhlker, C., Massabò, D., Brito, J., Carbone, S., Cheng, Y., Chi, X., Ditas, F., Hrabě de
686 Angelis, I., Morán-Zuloaga, D., Pöhlker, M. L., Rizzo, L. V., Walter, D., Wang, Q., Artaxo, P., Prati,
687 P., and Andreae, M. O.: Comparison of different Aethalometer correction schemes and a reference
688 multi-wavelength absorption technique for ambient aerosol data, *Atmos. Meas. Tech. Discuss.*,
689 doi:10.5194/amt-2016-361, in review, 2016.

690 Schladitz, A., Müller, T., Kaaden, N., Massling, A., Kandler, K., Ebert, M., Weinbruch, S., Deutscher,
691 C., and Wiedensohler, A.: In situ measurements of optical properties at Tinfou (Morocco) during the
692 Saharan Mineral Dust Experiment SAMUM 2006, *Tellus B*, 61, 64–78, doi:10.1111/j.1600-
693 0889.2008.00397.x, 2009.

694 Schmid, O., Artaxo, P., Arnott, W. P., Chand, D., Gatti, L. V., Frank, G. P., Hoffer, A., Schnaiter, M.,
695 and Andreae, M. O.: Spectral light absorption by ambient aerosols influenced by biomass burning in
696 the Amazon Basin. I: Comparison and field calibration of absorption measurement techniques,
697 *Atmos. Chem. Phys.*, 6, 3443–3462, 2006.

698 Segura, S., Estellés, V., Titos, G., Lyamani, H., Utrillas, M. P., Zotter, P., Prévôt, A. S. H., Močnik, G.,
699 Alados-Arboledas, L., and Martínez-Lozano, J. A.: Determination and analysis of in situ spectral
700 aerosol optical properties by a multi-instrumental approach, *Atmos. Meas. Tech.*, 7, 2373-2387, doi:
701 10.5194/amt-7-2373-2014, 2014.

702 Sherman, J. P., Sheridan, P. J., Ogren, J. A., Andrews, E., Hageman, D., Schmeisser, L., Jefferson,
703 A., and Sharma, S.: A multi-year study of lower tropospheric aerosol variability and systematic
704 relationships from four North American regions, *Atmos. Chem. Phys.*, 15, 12487-12517,
705 doi:10.5194/acp-15-12487-2015, 2015.

- 706 Slingo, A., et al., Observations of the impact of a major Saharan dust storm on the atmospheric
707 radiation balance, *Geophys. Res. Lett.*, 33, L24817, doi:10.1029/2006GL027869, 2006.
- 708 Sokolik, I., and Toon, O.: Incorporation of mineralogical composition into models of the radiative
709 properties of mineral aerosol from UV to IR wavelengths, *J. Geophys. Res.*, 104, 9423-9444, 1999.
- 710 Solmon, F., Mallet, M., Elguindi, N., Giorgi, F., Zakey, A. and Konaré, A.: Dust aerosol impact on
711 regional precipitation over western Africa, mechanisms and sensitivity to absorption properties,
712 *Geophys. Res. Lett.*, 35, L24705, doi:10.1029/2008GL035900, 2008.
- 713 Toon, O. B., Pollack, J. B., and Khare, B. N.: The Optical Constants of Several Atmospheric Aerosol
714 Species: Ammonium Sulfate, Aluminum Oxide, and Sodium Chloride, *J. Geophys. Res.*, 81, 5733–
715 5748, 1976.
- 716 Utry, N., Ajtai, T., Pintér, M., Tombácz, E., Illés, E., Bozóki, Z., and Szabó, G.: Mass-specific optical
717 absorption coefficients and imaginary part of the complex refractive indices of mineral dust
718 components measured by a multi-wavelength photoacoustic spectrometer, *Atmos. Meas. Tech.*, 8,
719 401-410, doi:10.5194/amt-8-401-2015, 2015.
- 720 Utry, N., Ajtai, T., Pintér, M. Illés, E., Tombácz, E., Szabó, G., and Bozóki, Z.: Generation and UV-
721 VIS-NIR spectral responses of organo-mineral aerosol for modelling soil derived dust, *Atmos.*
722 *Environ.*, 152, 553-561, 2017.
- 723 Virkkula, A., Makela, T., Hillamo, R., Yli-Tuomi, T., Hirsikko, A., Hameri, K., and Koponen, I. K.: A
724 simple procedure for correcting loading effects of aethalometer data, *J. Air Waste Manage.*, 57(10),
725 1214–1222, 2007.
- 726 von der Weiden, S.-L., Drewnick, F., and Borrmann, S.: Particle Loss Calculator – a new software tool
727 for the assessment of the performance of aerosol inlet systems, *Atmos. Meas. Tech.*, 2, 479–494,
728 2009.
- 729 Weingartner, E., Saathof, H., Schnaiter, M., Streit, N., Bitnar, B., and Baltensperger, U.: Absorption of
730 light by soot particles: Determination of the absorption coefficient by means of Aethalometers, *J.*
731 *Aerosol Sci.*, 34, 1445–1463, 2003.
- 732 Yoshioka, M., N.M.Mahowald, A. J. Conley, W. D. Collins, D.W. Fillmore, C. S. Zender, and D. B.
733 Coleman: Impact of desert dust radiative forcing on sahel precipitation: Relative importance of dust
734 compared to sea surface temperature variations, vegetation changes, and greenhouse gas
735 warming, *J. Clim.*, 20, 1445– 1467, 2007.

736 **Table captions**

737 **Table 1.** Specifications and references of instruments used during experiments.

738 **Table 2.** Summary of experiments and results. The mean and the standard deviation of $D_{\text{eff, fine}}$,
739 $D_{\text{eff, coarse}}$, SSA at 450 and 660 nm, C_{ref}^* , $C_{\text{ref}}(\text{W2003})$, and $C_{\text{ref}}(\text{C2010})$ are reported. As a reminder:
740 C_{ref}^* is the multiple scattering correction obtained not taking into account the loading effect correction
741 in aethalometer data; $C_{\text{ref}}(\text{W2003})$ and $C_{\text{ref}}(\text{C2010})$ take the loading effect correction into account, by
742 using the parametrisations by Weingartner et al. (2003) (referred as W2003) and Collaud Coen et al.
743 (2010) (referred as C2010), respectively. The maximum of the % difference between C_{ref}^* ,
744 $C_{\text{ref}}(\text{W2003})$, and $C_{\text{ref}}(\text{C2010})$ is indicated in the table.

745 **Table 3.** Mean and standard deviation multiple scattering correction $\overline{C_{\text{ref}}}$ at 450 and 660 nm for dust,
746 kaolinite, and ambient air. The $\overline{C_{\text{ref}}}$ was calculated as the mean of the C_{ref}^* , $C_{\text{ref}}(\text{W2003})$, and
747 $C_{\text{ref}}(\text{C2010})$ obtained at each wavelength for the different aerosol types. As a reminder: C_{ref}^* is the
748 multiple scattering correction obtained not taking into account the loading effect correction in
749 aethalometer data; $C_{\text{ref}}(\text{W2003})$ and $C_{\text{ref}}(\text{C2010})$ take the loading effect correction into account, by
750 using the parametrisations by Weingartner et al. (2003) and Collaud Coen et al. (2010), respectively.

751

752 **Figure captions**

753 **Figure 1.** Experimental setup used for the aethalometer intercomparison experiments.

754 **Figure 2.** Temporal series of experiments showing the measured optical data at 660 nm. The different
755 panels show (from the top to the bottom): (i) the loading-corrected aethalometer attenuation at 660
756 nm (data corrected with the R formulation by Collaud Coen et al. (2010) (referred to as R(C2010)) are
757 shown) and the MAAP aerosol absorption coefficient; (ii) the aerosol extinction at 660 nm
758 extrapolated from CAPS PMex measurements and estimated as the sum of nephelometer scattering
759 and MAAP absorption; (iii) the extinction aerosol Ångstrom exponent; (iv) the aerosol single scattering
760 albedo at 660 nm. Each point in the plot corresponds to 2 min average data. The x-axis indicates the
761 data point sequential number. Experiments with dust samples and kaolinite occurred between the 3rd
762 and the 9th of November 2016 and lasted between 1 and 2 hours each. Ambient air data were
763 collected at different steps between the 8th and the 14th November 2016 for a total of 7 hours of
764 measurements.

765 **Figure 3.** Ammonium sulfate experiment. Left panel: temporal evolution of the extinction and
766 scattering coefficients measured by the CAPS PMex and the nephelometer at 450 nm (blue scale)
767 and 630 nm (red scale). Each point in the plot corresponds to 2 min average data. Right panel: CAPS
768 PMex versus nephelometer data (10 minutes averages). The $y=x$ line and the results of the linear fit
769 between CAPS and nephelometer data are also shown in the plot.

770 **Figure 4.** CAPS PMex extinction coefficient extrapolated at 660 nm versus nephelometer+MAAP
771 calculated extinction at 660 nm for all experiments (dust, kaolinite, ambient air). Each point in the plot

772 corresponds to 10 min average data. The $y=x$ line and the results of the linear fit between CAPS and
773 nephelometer+MAAP data are also shown in the plot.

774 **Figure 5.** Left panel: estimated f values versus $(1-SSA)$ at 660 nm for dust aerosols. Different
775 symbols are used to distinguish between dust from different sources. The uncertainty of $(1-SSA)$ is
776 the standard deviation over 2-min data, while that of f is calculated with the error propagation formula
777 taking into account the uncertainty of a (± 0.14) and that of $(1-SSA)$. Right panel: f versus SSA at 660
778 nm for all experiments. Different symbols are used to distinguish between different aerosol types. The
779 results of the linear fit between f and $(1-SSA)$ are also reported. Data from Weingartner et al. (2003)
780 (W2003) (extracted from their Figure 4) are also shown in the plot for comparison.

781 **Figure 6.** Top panel: $C_{ref}(W2003)$ (multiple scattering correction obtained by taking into account the
782 loading effect correction using the parametrisations by Weingartner et al. (2003)) versus SSA at 450
783 and 660 nm for mineral dust samples analysed in this study. Different symbols are used to distinguish
784 between dust from different sources. As indicated in Table 2, the difference between C_{ref}^* ,
785 $C_{ref}(W2003)$, and $C_{ref}(C2010)$ is very low for mineral dust aerosols. The uncertainty of SSA is the
786 standard deviation over 2-min data, while that of $C_{ref}(W2003)$ is calculated with the error propagation
787 formula taking into account the uncertainty of $\beta_{abs,ref}$ and that of $\beta_{ATT}/R(W2003)$. Bottom panel: C_{ref}
788 versus SSA at 450 and 660 nm for the different aerosol samples analysed in this study. Different
789 symbols are used to distinguish between different aerosol types. Data for both $C_{ref}(W2003)$ and C_{ref}^*
790 (multiple scattering correction obtained not taking into account the loading effect correction in
791 aethalometer data) are shown for ambient air aerosols, while for dust and kaolinite, for which the
792 difference between the different formulations is very low, only $C_{ref}(W2003)$ is reported. Data from
793 Weingartner et al. (2003) (W2003) (C_{ref} from their Table 3, and SSA extracted from their Fig. 4) and
794 Collaud Coen et al. (2010) (C2010) (extracted from their Fig. 5) at 660 nm are also shown in the plot
795 for comparison. The results of the linear fits between C_{ref} and SSA for mineral dust and for the entire
796 dataset are also shown in the plot.

797 **Figure 7.** Examples of number size distribution (normalised to the total number concentration) for
798 ammonium sulfate, dust (Niger sample), kaolinite, and ambient air aerosols. Data refer to the mean
799 over each experiment as measured from the SMPS and the OPC. Error bars (standard deviations)
800 have been omitted for the sake of clarity.

801 **Figure 8.** Top panel: $C_{ref}(W2003)$ (multiple scattering correction obtained by taking into account the
802 loading effect correction using the parametrisations by Weingartner et al. (2003)) at 450 and 660 nm
803 versus the effective diameter coarse $D_{eff,coarse}$ for mineral dust samples analysed in this study.
804 Different symbols are used to distinguish between dust from different sources. The uncertainty of
805 $D_{eff,coarse}$ is the standard deviation over 2-min data, while that of $C_{ref}(W2003)$ is calculated with the
806 error propagation formula taking into account the uncertainty of $\beta_{abs,ref}$ and that of $\beta_{ATT}/R(W2003)$.
807 Bottom panel: C_{ref} at 450 and 660 nm versus the effective diameter coarse $D_{eff,coarse}$ for the different
808 aerosol samples analysed in this study. Different symbols are used to distinguish between different
809 aerosol types. Data for both $C_{ref}(W2003)$ and C_{ref}^* (multiple scattering correction obtained not taking
810 into account the loading effect correction in aethalometer data) are shown for ambient air aerosols,

811 while for dust and kaolinite, for which the difference between the different formulations is very low,
812 only $C_{\text{ref}}(\text{W2003})$ is reported. The results of the linear fits between C_{ref} and $D_{\text{eff,coarse}}$ for mineral dust
813 and for the entire dataset are also shown in the plot.

814

815 **Table 1.** Specifications and references of instruments used during experiments.

Instrument	Property	Operating wavelength (nm)	Time resolution	Flowrate (L min ⁻¹)	Percent uncertainty	Reference
Aethalometer (model AE-31, Magee Sci.)	Spectral absorption coefficient	370, 470, 520, 590, 660, 880, 950	2 min	8	±20% (attenuation coefficient)	Hansen et al. (1984); W2003; C2010
Multi-Angle Absorption Photometer (MAAP, model 5012, Thermo Sci.)	Single-wavelength absorption coefficient	670	1 min	8	±12%	Petzold and Schönlinner (2004); Petzold et al. (2005)
Cavity Attenuated Phase Shift Extinction (CAPS PMex, Aerodyne)	Spectral extinction coefficient	450, 630	1 s	0.85	±5%	Massoli et al. (2010)
Nephelometer (model 3563, TSI Inc.)	Spectral scattering coefficient	450, 550, 700	1 s	18	±~9%	Sherman et al. (2015)
SMPS (DMA model 3080, CPC model 3772, TSI Inc.)	Number size distribution	–	3 min	2	–	De Carlo et al. (2004)
OPC optical particle counter (model 1.109, Grimm Inc.)	Number size distribution	655	6 s	1.2	±15% (diameter optical to geometric conversion); ±10 (concentration)	Heim et al. (2008)

816

817

818 **Table 2.** Summary of experiments and results. The mean and the standard deviation of $D_{\text{eff, fine}}$,
819 $D_{\text{eff, coarse}}$, SSA at 450 and 660 nm, C_{ref}^* , $C_{\text{ref}}(\text{W2003})$, and $C_{\text{ref}}(\text{C2010})$ are reported. As a reminder:
820 C_{ref}^* is the multiple scattering correction obtained not taking into account the loading effect correction
821 in aethalometer data; $C_{\text{ref}}(\text{W2003})$ and $C_{\text{ref}}(\text{C2010})$ take the loading effect correction into account, by
822 using the parametrisations by Weingartner et al. (2003) (referred as W2003) and Collaud Coen et al.
823 (2010) (referred as C2010), respectively. The maximum of the % difference between C_{ref}^* ,
824 $C_{\text{ref}}(\text{W2003})$, and $C_{\text{ref}}(\text{C2010})$ is indicated in the table.

Aerosol ID	Source	$D_{\text{eff, fine}} (\mu\text{m})$ $D_{\text{eff, coarse}} (\mu\text{m})$	SSA 450 nm 660 nm	C_{ref}^* 450 nm 660 nm	$C_{\text{ref}}(\text{W2003})$ 450 nm 660 nm	$C_{\text{ref}}(\text{C2010})$ 450 nm 660 nm	Max % diff C_{ref}^* 450 nm 660 nm
Ammonium sulfate	Sigma-Aldrich 99.999% purity	–	$0.999 \pm (<)0.001$ $0.999 \pm (<)0.001$		–	–	
Niger 1	Sahel (13.52°N, 2.63°E)	0.38 ± 0.01 2.6 ± 0.1	0.93 ± 0.01 0.98 ± 0.01	2.00 ± 0.45 1.87 ± 0.51	2.01 ± 0.45 1.87 ± 0.51	2.02 ± 0.45 1.88 ± 0.51	1.0 % 0.4 %
Niger 2	Sahel (13.52°N, 2.63°E)	0.32 ± 0.02 2.3 ± 0.1	0.92 ± 0.01 0.98 ± 0.01	2.05 ± 0.46 1.89 ± 0.57	2.11 ± 0.47 1.92 ± 0.56	2.10 ± 0.47 1.92 ± 0.57	2.8 % 1.6 %
China	Gobi desert (39.43°N, 105.67°E)	0.44 ± 0.01 3.1 ± 0.2	0.94 ± 0.01 0.98 ± 0.01	2.15 ± 0.48 2.02 ± 0.62	2.16 ± 0.48 2.01 ± 0.62	2.16 ± 0.48 2.02 ± 0.63	0.5 % 0.3 %
Arizona	Sonoran desert (33.15°N, 112.08°W)	0.53 ± 0.02 3.1 ± 0.2	0.96 ± 0.01 0.99 ± 0.01	1.81 ± 0.40 1.76 ± 0.56	1.82 ± 0.41 1.78 ± 0.55	1.82 ± 0.41 1.78 ± 0.57	0.5 % 1.1 %
Tunisia	Sahara desert (33.02°N, 10.67°E)	0.48 ± 0.03 3.2 ± 0.7	0.96 ± 0.01 0.99 ± 0.01	1.97 ± 0.49 1.80 ± 0.42	1.98 ± 0.44 1.80 ± 0.42	1.98 ± 0.44 1.80 ± 0.42	0.5 % 0 %
Australia	Strzelecki desert (31.33°S, 140.33°E)	0.55 ± 0.02 2.4 ± 0.1	0.85 ± 0.01 0.98 ± 0.01	2.52 ± 0.56 2.28 ± 0.74	2.56 ± 0.57 2.26 ± 0.72	2.56 ± 0.57 2.28 ± 0.74	1.6 % 0.9 %
Namibia	Namib desert (19.0°S, 13.0°E)	0.45 ± 0.04 3.6 ± 0.3	0.95 ± 0.01 0.98 ± 0.01	2.02 ± 0.45 1.75 ± 0.57	2.03 ± 0.45 1.76 ± 0.54	2.03 ± 0.45 1.79 ± 0.57	0.5 % 2.2 %
Kaolinite	Source Clay Repository KGa-2	0.39 ± 0.07 2.3 ± 1.6	0.96 ± 0.01 0.97 ± 0.01	2.47 ± 0.55 2.31 ± 0.60	2.51 ± 0.56 2.34 ± 0.60	2.50 ± 0.56 2.33 ± 0.60	1.6 % 1.3 %
Ambient air 1	Suburbs of Paris	0.24 ± 0.08 5.2 ± 0.9	0.79 ± 0.05 0.61 ± 0.08	3.87 ± 0.87 1.97 ± 0.71	4.01 ± 0.90 2.05 ± 0.73	4.03 ± 0.90 2.11 ± 0.76	4.0 % 6.6 %
Ambient air 2	Suburbs of Paris	0.50 ± 0.02 4.5 ± 0.1	0.72 ± 0.04 0.67 ± 0.09	3.22 ± 0.72 1.66 ± 0.44	3.68 ± 0.82 1.94 ± 0.52	3.57 ± 0.80 1.87 ± 0.50	12.5 % 14.4 %
Ambient air 3	Suburbs of Paris	0.46 ± 0.03 6.2 ± 0.7	0.78 ± 0.06 0.54 ± 0.10	3.93 ± 0.88 2.32 ± 0.76	4.35 ± 0.97 2.78 ± 0.89	4.25 ± 0.95 2.68 ± 0.87	21.1 % 16.5 %
Ambient air 4	Suburbs of Paris	0.53 ± 0.05 5.3 ± 1.3	0.63 ± 0.05 0.42 ± 0.08	3.41 ± 0.76 2.25 ± 0.68	3.90 ± 0.87 2.69 ± 0.81	3.79 ± 0.85 2.62 ± 0.79	12.6 % 16.4 %
Ambient air 5	Suburbs of Paris	0.37 ± 0.03 3.4 ± 0.1	0.76 ± 0.08 0.65 ± 0.12	2.72 ± 0.61 2.54 ± 0.82	2.58 ± 0.58 2.51 ± 0.81	2.77 ± 0.62 2.61 ± 0.85	5.4 % 2.7 %
Ambient air 6	Suburbs of Paris	0.37 ± 0.05 4.1 ± 1.0	0.62 ± 0.04 0.46 ± 0.09	2.75 ± 0.50 2.24 ± 0.60	2.78 ± 0.62 2.96 ± 0.79	2.66 ± 0.59 2.79 ± 0.75	19.1 % 24.3 %
Ambient air 7	Suburbs of Paris	0.40 ± 0.01 4.7 ± 0.7	0.87 ± 0.05 0.76 ± 0.08	3.85 ± 0.86 1.86 ± 0.74	4.06 ± 0.91 2.04 ± 0.69	4.01 ± 0.90 2.02 ± 0.80	5.2 % 8.8 %
Ambient air 8	Suburbs of Paris	0.42 ± 0.07 4.3 ± 0.7	0.78 ± 0.06 0.71 ± 0.07	1.91 ± 0.43 2.09 ± 0.61	2.22 ± 0.50 2.53 ± 0.73	2.16 ± 0.48 2.45 ± 0.72	14.0 % 17.4 %

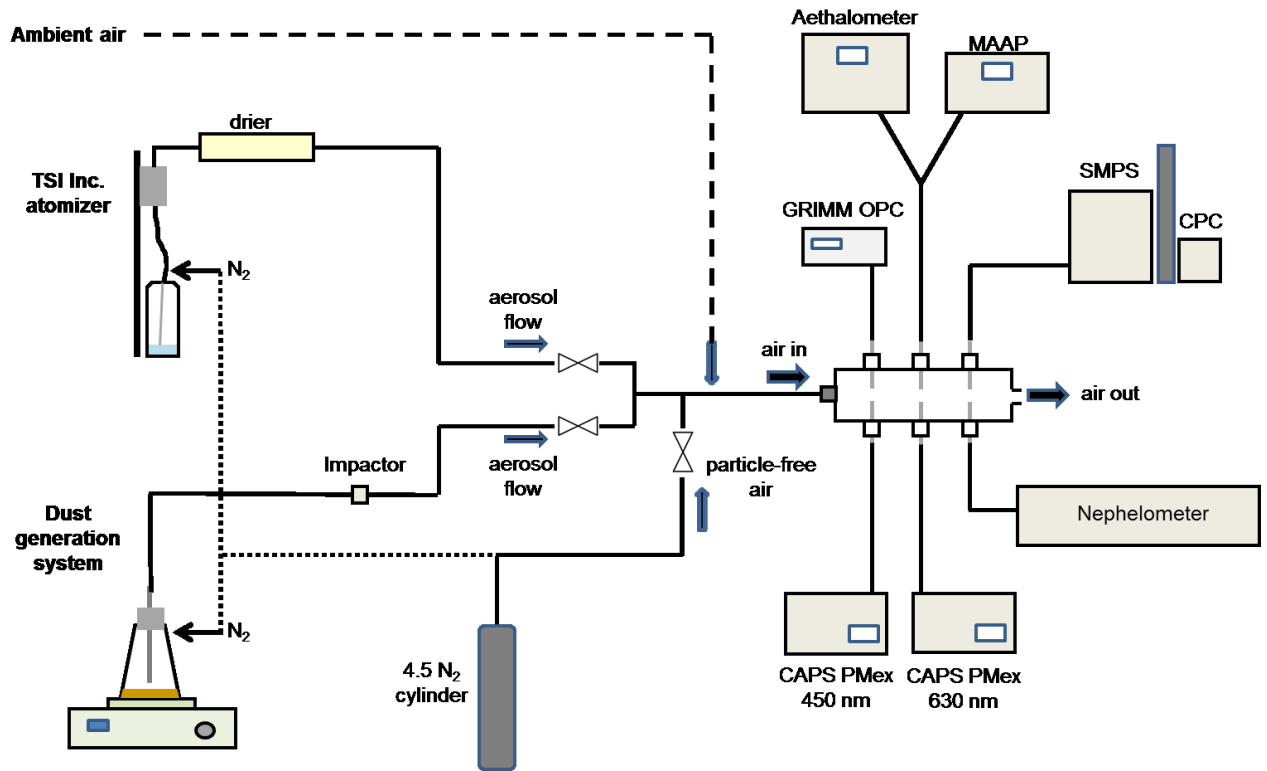
825 **Table 3.** Mean and standard deviation multiple scattering correction $\overline{C_{ref}}$ at 450 and 660 nm for dust,
826 kaolinite, and ambient air. The $\overline{C_{ref}}$ was calculated as the mean of the C_{ref}^* , $C_{ref}(W2003)$, and
827 $C_{ref}(C2010)$ obtained at each wavelength for the different aerosol types. As a reminder: C_{ref}^* is the
828 multiple scattering correction obtained not taking into account the loading effect correction in
829 aethalometer data; $C_{ref}(W2003)$ and $C_{ref}(C2010)$ take the loading effect correction into account, by
830 using the parametrisations by Weingartner et al. (2003) and Collaud Coen et al. (2010), respectively.
831

	$\overline{C_{ref}}$	
	450 nm	660 nm
Mineral dust	2.09 ± 0.22	1.92 ± 0.17
Kaolinite	2.49 ± 0.02	2.31 ± 0.02
Ambient air	3.31 ± 0.75	2.32 ± 0.35

832

833

834 **Figure 1.** Experimental setup used for the aethalometer intercomparison experiments.



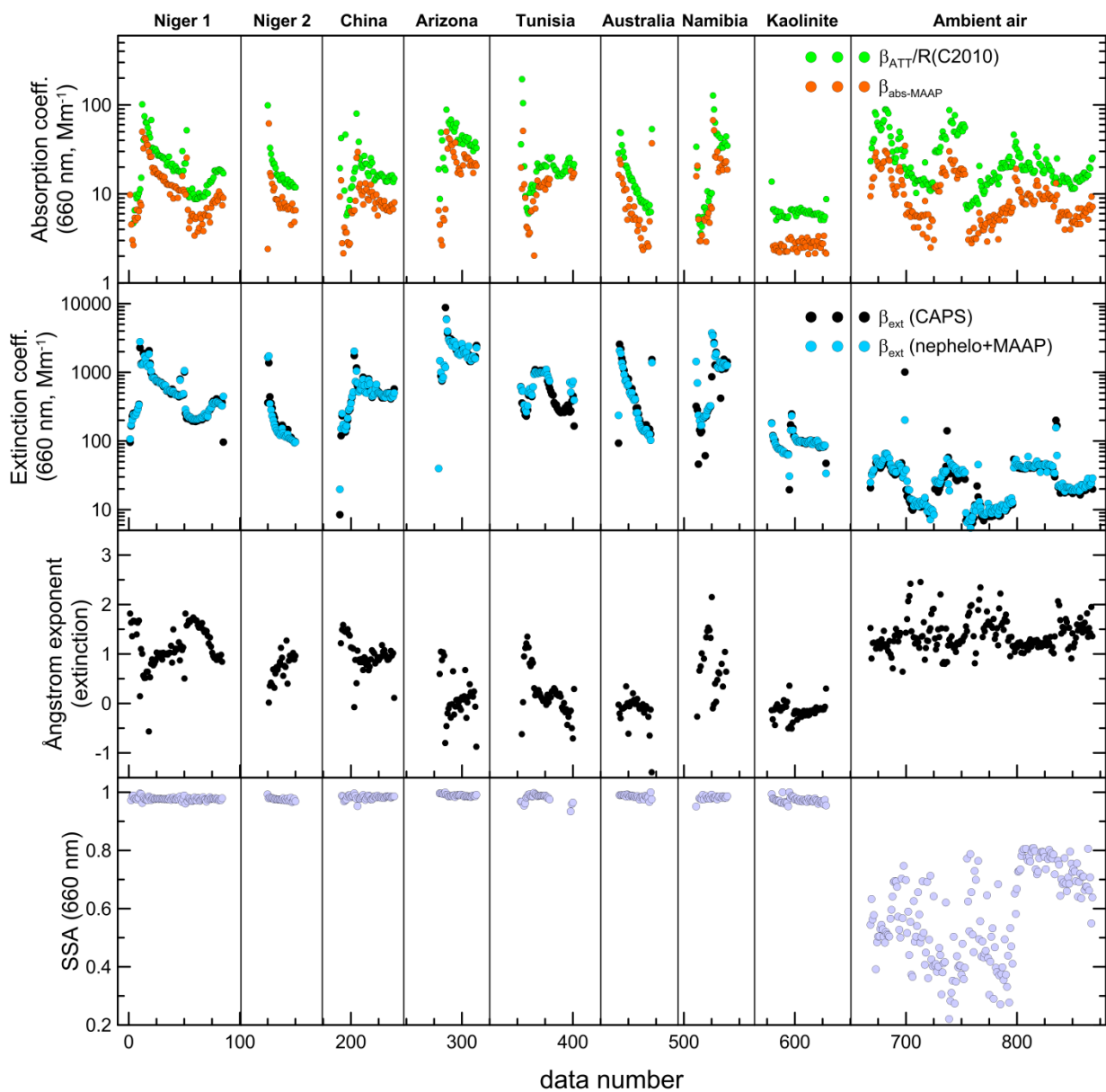
835
836

837

838

839 **Figure 2.** Temporal series of experiments showing the measured optical data at 660 nm. The different
 840 panels show (from the top to the bottom): (i) the loading-corrected aethalometer attenuation at 660
 841 nm (data corrected with the R formulation by Collaud Coen et al. (2010) (referred to as R(C2010)) are
 842 shown) and the MAAP aerosol absorption coefficient; (ii) the aerosol extinction at 660 nm
 843 extrapolated from CAPS PMex measurements and estimated as the sum of nephelometer scattering
 844 and MAAP absorption; (iii) the extinction aerosol Ångstrom exponent; (iv) the aerosol single scattering
 845 albedo at 660 nm. Each point in the plot corresponds to 2 min average data. The x-axis indicates the
 846 data point sequential number. Experiments with dust samples and kaolinite occurred between the 3rd
 847 and the 9th of November 2016 and lasted between 1 and 2 hours each. Ambient air data were
 848 collected at different steps between the 8th and the 14th November 2016 for a total of 7 hours of
 849 measurements.

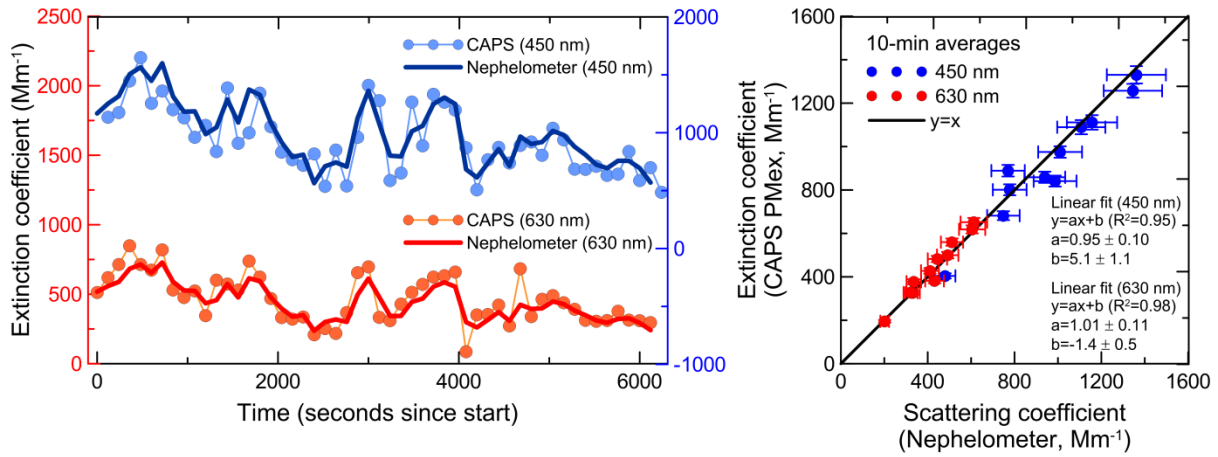
850



851
852

853 **Figure 3.** Ammonium sulfate experiment. Left panel: temporal evolution of the extinction and
854 scattering coefficients measured by the CAPS PMex and the nephelometer at 450 nm (blue scale)
855 and 630 nm (red scale). Each point in the plot corresponds to 2 min average data. Right panel: CAPS
856 PMex versus nephelometer data (10 minutes averages). The $y=x$ line and the results of the linear fit
857 between CAPS and nephelometer data are also shown in the plot.

858
859

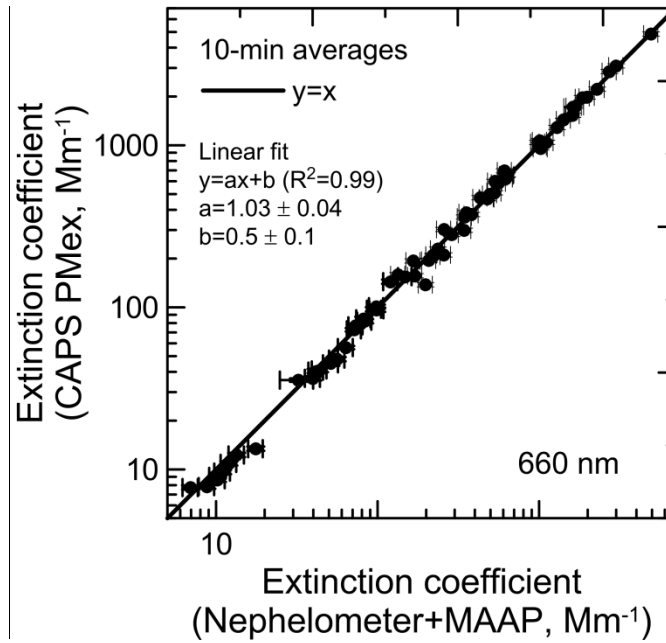


860

861

862 **Figure 4.** CAPS PMex extinction coefficient extrapolated at 660 nm versus nephelometer+MAAP
863 calculated extinction at 660 nm for all experiments (dust, kaolinite, ambient air). Each point in the plot
864 corresponds to 10 min average data. The y=x line and the results of the linear fit between CAPS and
865 nephelometer+MAAP data are also shown in the plot.

866



867

868

869

870

871

872

873

874

875

876

877

878

879

880

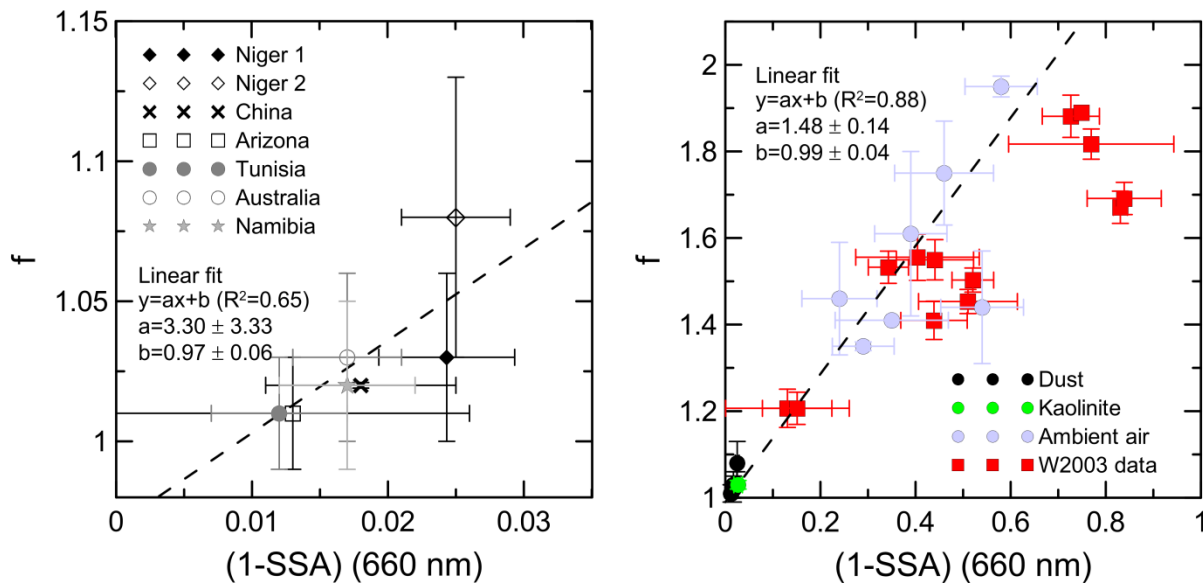
881

882

883

884 **Figure 5.** Left panel: estimated f values versus $(1-SSA)$ at 660 nm for dust aerosols. Different
 885 symbols are used to distinguish between dust from different sources. The uncertainty of $(1-SSA)$ is
 886 the standard deviation over 2-min data, while that of f is calculated with the error propagation formula
 887 taking into account the uncertainty of a (± 0.14) and that of $(1-SSA)$. Right panel: f versus SSA at 660
 888 nm for all experiments. Different symbols are used to distinguish between different aerosol types. The
 889 results of the linear fit between f and $(1-SSA)$ are also reported. Data from Weingartner et al. (2003)
 890 (W2003) (extracted from their Figure 4) are also shown in the plot for comparison.

891
 892
 893

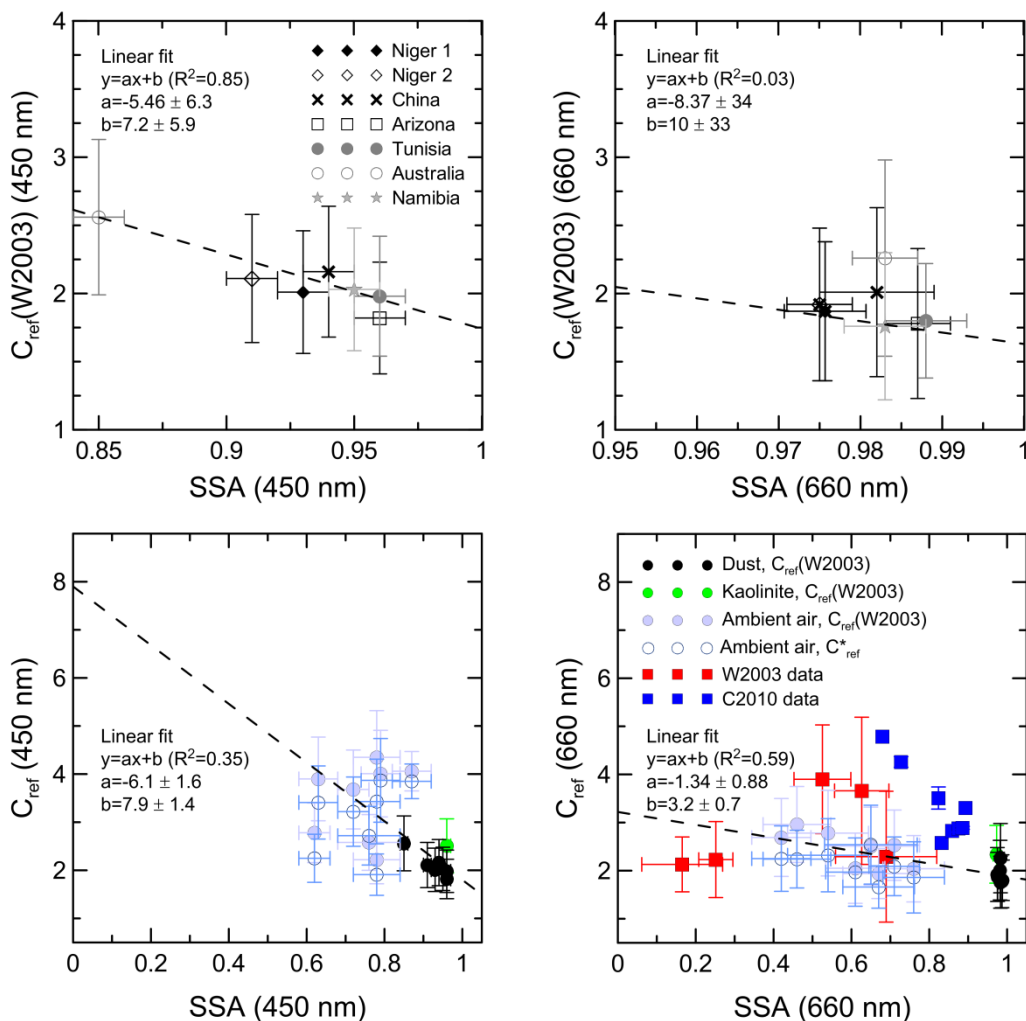


894
 895

896 **Figure 6.** Top panel: $C_{ref}(W2003)$ (multiple scattering correction obtained by taking into account the
 897 loading effect correction using the parametrisations by Weingartner et al. (2003)) versus SSA at 450
 898 and 660 nm for mineral dust samples analysed in this study. Different symbols are used to distinguish
 899 between dust from different sources. As indicated in Table 2, the difference between C_{ref}^* ,
 900 $C_{ref}(W2003)$, and $C_{ref}(C2010)$ is very low for mineral dust aerosols. The uncertainty of SSA is the
 901 standard deviation over 2-min data, while that of $C_{ref}(W2003)$ is calculated with the error propagation
 902 formula taking into account the uncertainty of $\beta_{abs,ref}$ and that of $\beta_{ATT}/R(W2003)$. Bottom panel: C_{ref}
 903 versus SSA at 450 and 660 nm for the different aerosol samples analysed in this study. Different
 904 symbols are used to distinguish between different aerosol types. Data for both $C_{ref}(W2003)$ and C_{ref}^*
 905 (multiple scattering fit correction obtained not taking into account the loading effect correction in
 906 aethalometer data) are shown for ambient air aerosols, while for dust and kaolinite, for which the
 907 difference between the different formulations is very low, only $C_{ref}(W2003)$ is reported. Data from
 908 Weingartner et al. (2003) (W2003) (C_{ref} from their Table 3, and SSA extracted from their Fig. 4) and
 909 Collaud Coen et al. (2010) (C2010) (extracted from their Fig. 5) at 660 nm are also shown in the plot
 910 for comparison. The results of the linear fits between C_{ref} and SSA for mineral dust and for the entire
 911 dataset are also shown in the plot.

912

913

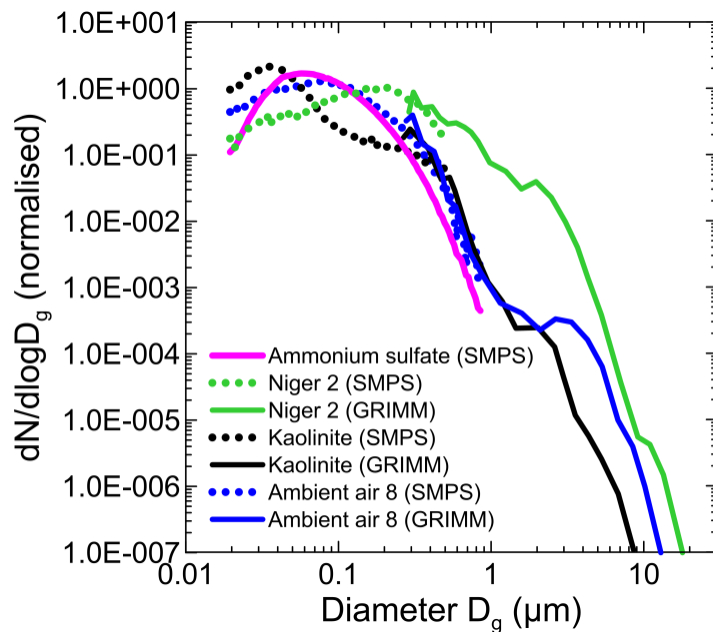


914

915

916 **Figure 7.** Examples of number size distribution (normalised to the total number concentration) for
917 ammonium sulfate, dust (Niger sample), kaolinite, and ambient air aerosols. Data refer to the mean
918 over each experiment as measured from the SMPS and the OPC. Error bars (standard deviations)
919 have been omitted for the sake of clarity.

920

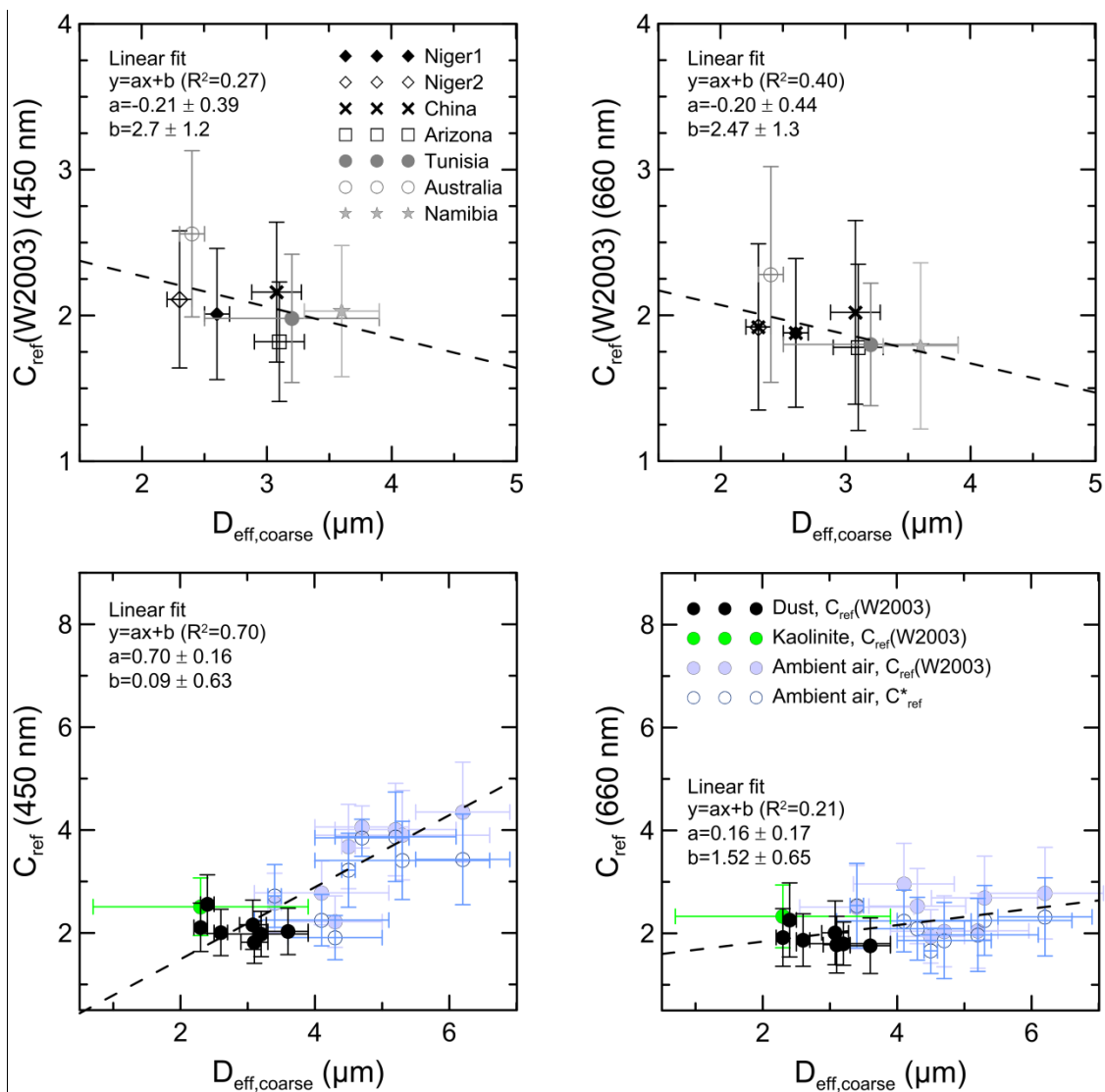


921

922

923 **Figure 8.** Top panel: $C_{ref}(W2003)$ (multiple scattering correction obtained by taking into account the
 924 loading effect correction using the parametrisations by Weingartner et al. (2003)) at 450 and 660 nm
 925 versus the effective diameter coarse $D_{eff,coarse}$ for mineral dust samples analysed in this study.
 926 Different symbols are used to distinguish between dust from different sources. The uncertainty of
 927 $D_{eff,coarse}$ is the standard deviation over 2-min data, while that of $C_{ref}(W2003)$ is calculated with the
 928 error propagation formula taking into account the uncertainty of $\beta_{abs,ref}$ and that of $\beta_{ATT}/R(W2003)$.
 929 Bottom panel: C_{ref} at 450 and 660 nm versus the effective diameter coarse $D_{eff,coarse}$ for the different
 930 aerosol samples analysed in this study. Different symbols are used to distinguish between different
 931 aerosol types. Data for both $C_{ref}(W2003)$ and C_{ref}^* (multiple scattering correction obtained not taking
 932 into account the loading effect correction in aethalometer data) are shown for ambient air aerosols,
 933 while for dust and kaolinite, for which the difference between the different formulations is very low,
 934 only $C_{ref}(W2003)$ is reported. The results of the linear fits between C_{ref} and $D_{eff,coarse}$ for mineral dust
 935 and for the entire dataset are also shown in the plot.

936



937